INTERNATIONAL JOURNAL FOR NUMERICAL METHODS IN FLUIDS
Int. J. Numer. Meth. Fluids 2009; **61**:1331–1362
Published online 30 January 2009 in Wiley InterScience (www.interscience.wiley.com). DOI: 10.1002/fld.2000

A volume-of-fluid method for incompressible free surface flows

I. R. Park*,†, K. S. Kim, J. Kim and S. H. Van

Marine Transportation System Laboratory, Maritime and Ocean Engineering Research Institute,
KORDI, Jang-dong 171, Yuseong-gu, Taejon 305-343, Korea

SUMMARY

This paper proposes a hybrid volume-of-fluid (VOF) level-set method for simulating incompressible two-phase flows. Motion of the free surface is represented by a VOF algorithm that uses high resolution differencing schemes to algebraically preserve both the sharpness of interface and the boundedness of volume fraction. The VOF method is specifically based on a simple order high resolution scheme lower than that of a comparable method, but still leading to a nearly equivalent order of accuracy. Retaining the mass conservation property, the hybrid algorithm couples the proposed VOF method with a level-set distancing algorithm in an implicit manner when the normal and the curvature of the interface need to be accurate for consideration of surface tension. For practical purposes, it is developed to be efficiently and easily extensible to three-dimensional applications with a minor implementation complexity. The accuracy and convergence properties of the method are verified through a wide range of tests: advection of rigid interfaces of different shapes, a three-dimensional air bubble's rising in viscous liquids, a two-dimensional dam-break, and a three-dimensional dam-break over an obstacle mounted on the bottom of a tank. The standard advection tests show that the volume advection algorithm is comparable in accuracy with geometric interface reconstruction algorithms of higher accuracy than other interface capturing-based methods found in the literature. The numerical results for the remainder of tests show a good agreement with other numerical solutions or available experimental data. Copyright © 2009 John Wiley & Sons, Ltd.

Received 9 September 2008; Revised 8 December 2008; Accepted 9 December 2008

KEY WORDS: two-phase flow; volume-of-fluid; Navier–Stokes equations; numerical methods; level-set distancing; finite volume method

---

*Correspondence to: I. R. Park, Marine Transportation System Laboratory, Maritime and Ocean Engineering Research Institute, KORDI, Jang-dong 171, Yuseong-gu, Taejon 305-343, Korea.

†E-mail: irpark@moeri.re.kr

Contract/grant sponsor: Ministry of Commerce, Industry, and Energy (MOCIE); contract/grant number: PNS116D
Contract/grant sponsor: MOERI/KORDI; contract/grant number: PES128A

Copyright © 2009 John Wiley & Sons, Ltd.

1. INTRODUCTION

A number of volume-of-fluid (VOF) algorithms have been proposed to accurately compute incompressible free surface flows since the introduction of the original VOF method [1]. During the last decades, applications of the VOF method [2–10] have been successfully carried out as well as those of the level-set method [11–14] in ship hydrodynamics and in many other industrial flow problems with the free surface. A broad review of various numerical methods for free surface flows can be found in [15]. There are different approaches to representing the interface using volume fractions, which can be classified into two categories: high resolution differencing scheme-based algorithms and geometric reconstruction-based algorithms. As known, the latter methods are based on an explicit Lagrangian advection algorithm using explicitly reconstructed interface segments. Most notable ones are a simple line interface calculation (SLIC) [16], a piecewise line interface calculation [17], and their variations [18–22] with several extensions for improvement. In the literature, most of the higher-order sharp interface methods for two-phase flows are extended from these volume tracking methods, since they explicitly represent the interface and treat its boundary conditions for improving the accuracy of volume fluxes and especially dynamic interface conditions, etc. However, it is often noted that geometric interface reconstruction-based methods have difficulties in extending to arbitrary irregular grids and three-dimensional computations owing to their algorithmic complexities. As an alternative to representing the interface, some volume tracking methods [8, 23–29] use high resolution schemes rather than a complicated geometric reconstruction process to calculate the volume fluxes. These methods are simple and implicit in the discretization process, but need a proper strategy that smoothly switches between downwind (DD) and upwind differencing (UD) schemes for preserving the physical volume fraction distribution and also for preventing numerical diffusion errors. Although there are several notable attempts made by using different types of high resolution schemes, the following three high resolution methods have been widely used in industrial fields: a high resolution interface capturing (HRIC) [8], a modified HRIC (MHRIC) [23], and a compressive interface capturing scheme for arbitrary meshes (CICSAM) [28]. Especially, the MHRIC, a modified version of the original HRIC scheme, is a VOF algorithm that combines its bounded downwind scheme with a bounded upwind scheme of third-order accuracy used by the CICSAM.

In recent years, the hybrid algorithms for coupling the level-set and the VOF methods also so called CLSVOF methods [30–34] have been attempted to effectively maintain mass conservation while providing improved accuracy in the interfacial normal and curvature calculations. In the CLSVOF methods, the interface is reconstructed using a volume tracking algorithm based on a complicated geometric process, while the continuous level-set function is used to calculate the interface normal and curvature. Specifically, the VOF function is used to correct the mass loss produced during the level-set re-distancing process. Instead of the level-set function, a higher-order volume fraction scheme can be used to calculate the interface curvature and maintain it to second-order accuracy [33]. However, although these methods are accurate in interface representation and in treatment of the interfacial boundary conditions, difficulties in implementing these models are still considerable and not easily extensible to three-dimensions.

In this paper, we propose a free surface method for simulating incompressible two-phase flows. The present work is based on a VOF advection algorithm that uses high resolution schemes. Furthermore, its algorithm couples the VOF and the level-set methods in a straightforward way when the interface normal and curvature need to be accurate for surface tension calculation. In the proposed method, the level-set function is temporarily constructed from the volume fractions

Copyright © 2009 John Wiley & Sons, Ltd.

DOI: 10.1002/fld

at every timestep without an additional advection of the level-set function, but no information from the level-set function has an explicit effect on the VOF values. For improving the mass conservation property of the constructed level-set function, we solve a level-set distancing equation with a fifth-order accurate scheme in space. The level-set function in the present implementation is used for calculating the local density and viscosity of the fluid as well as the interface normal and curvature. The proposed method is extended to three-dimensional structured grids and can be also extensible to multi-dimensional unstructured grids with a minor complexity and with a specific strategy as shown in [28].

In the remainder of this paper, we provide details on numerical implementations for the governing equations and free surface representations. In the numerical results section, we consider three groups of test subjects for validation. The accuracy of the present VOF advection algorithm is analyzed in the first validation examples: rigid translation and rotation of interfaces of different shapes. In the applications to a three-dimensional air bubble's rising in viscous liquids with a large density ratio, we prove the accuracy and convergence of the present hybrid algorithm by comparing the results with other numerical results found in the literature. Finally, the present free surface algorithm was applied to violent free surface flows interacting with structures: a two-dimensional dam-break and a three-dimensional dam-break over an obstacle mounted on the bottom of a tank. For validation, we compared the free surface elevations and violent impacts of water on fixed structures with available experimental data. In addition to these comparisons, we show the local flow behavior of deforming water front under the influence of viscous boundary layers, which has not been yet shown for dam-break problems in the literature.

2. MATHEMATICAL MODEL

2.1. Governing equations

For incompressible two-phase flows, a single set of the mass and the Navier–Stokes momentum conservation equations with variable properties are written in the integral form as

$$\int_S \mathbf{v}\cdot\mathbf{n}\,\mathrm{d}S = 0 \tag{1}$$

$$\frac{\partial}{\partial t}\int_\Omega \rho u_i\,\mathrm{d}\Omega + \int_S \rho u_i \mathbf{v}\cdot\mathbf{n}\,\mathrm{d}S = -\int_S p\mathbf{i}_i\cdot\mathbf{n}\,\mathrm{d}S + \int_S \tau_{ij}\mathbf{i}_j\cdot\mathbf{n}\,\mathrm{d}S + \int_\Omega f_{\sigma i}\,\mathrm{d}\Omega + \int_\Omega \rho g_i\,\mathrm{d}\Omega \tag{2}$$

in which S is the closed surface bounding a control volume (CV) Ω, $\mathbf{v}$ is the velocity vector whose Cartesian components are u_i in the direction of the Cartesian coordinate x_i, $\mathbf{n}$ is the unit normal vector to S, t is time, ρ is the density, p is the static pressure, $f_{\sigma i}$ is the external body force due to surface tension, and g_i is the gravitational acceleration. The viscous stress tensor τ_{ij} is given by

$$\tau_{ij} = \mu\left(\frac{\partial u_i}{\partial x_j} + \frac{\partial u_j}{\partial x_i}\right) \tag{3}$$

where μ is the molecular kinematic viscosity and δ_{ij} is the Kronecker delta. If one solves turbulent flows, it can be assumed that the flows are governed by the Reynolds-averaged Navier–Stokes and continuity equations. The averaged stress tensor $\bar{\tau}_{ij}$ in the momentum equations, which contains

Copyright © 2009 John Wiley & Sons, Ltd.

the Reynolds stress term, can be approximated by using Boussinesq's isotropic eddy viscosity hypothesis as follows:

$$\bar{\tau}_{ij}=\mu_{\mathrm{e}}\left(\frac{\partial \bar{u}_i}{\partial x_j}+\frac{\partial \bar{u}_j}{\partial x_i}\right)-\frac{2}{3}\delta_{ij}k \tag{4}$$

where $\bar{u}_i$ denotes the Reynolds-averaged velocity vector, k is the turbulent kinetic energy, and μ_{e} is an effective viscosity, i.e. the sum of turbulent eddy viscosity μ_{t} and molecular kinematic viscosity μ

$$\mu_{\mathrm{e}}=\mu_{\mathrm{t}}+\mu \tag{5}$$

To calculate the turbulent eddy viscosity μ_{t}, we use the standard k–ε model [35] with the so-called Launder and Spalding's wall function [35] that bridges the fully turbulent region and the wall.

If one defines motions of the interface using a volume fraction field, the resulting VOF equation is described as

$$\frac{\partial}{\partial t}\int_{\Omega}\alpha\,\mathrm{d}\Omega+\int_{S}\alpha\mathbf{v}\cdot\mathbf{n}\,\mathrm{d}S=0 \tag{6}$$

where α denotes the volume fraction, which is equal to 1 in the liquid and 0 in the gas. The interface is then represented by the volume fraction values, $0<\alpha<1$ Since the interface is time-dependent and advected with the flow field, note that a VOF advection algorithm is needed to be implemented to solve Equation (6). When considering surface tension, we temporarily construct a smooth level-set function, ϕ, from the volume fraction to improve the accuracy of the interface normal and curvature calculations. The detailed implementation algorithm will be demonstrated in the next section. The surface tension effects can be approximated in the momentum equations by using the continuum surface force model [36] expressed as

$$f_{\sigma i}=\sigma\kappa\nabla H(\phi) \tag{7}$$

with

$$\kappa=\nabla\cdot\frac{\nabla\phi}{|\nabla\phi|} \tag{8}$$

$$H(\phi)=\begin{Bmatrix}1 & \text{where } \phi\geqslant 0\\ 0 & \text{elsewhere}\end{Bmatrix} \tag{9}$$

where σ is the surface tension coefficient, κ is the curvature of the interface, and $H(\phi)$ is a Heaviside function. Here, the density and viscosity are determined on the basis of the level-set function as

$$\rho(\phi)=H(\phi)\rho_l+(1-H(\phi))\rho_g \tag{10}$$

$$\mu(\phi)=H(\phi)\mu_l+(1-H(\phi))\mu_g \tag{11}$$

where the subscripts l and g denote the liquid and the gas, respectively. If the level-set construction process for considering surface tension effects is unnecessary, the local density and viscosity of

Copyright © 2009 John Wiley & Sons, Ltd.

the fluid can be defined using the volume fraction instead of the level-set function as follows:

$$\rho(\alpha)=\alpha\rho_l+(1-\alpha)\rho_g \tag{12}$$

$$\mu(\alpha)=\alpha\mu_l+(1-\alpha)\mu_g \tag{13}$$

2.2. *VOF interface model*

In discretizing the advection equation, (6), for the volume fraction, the main difficulty is associated with the selection of an appropriate interpolation scheme that guarantees both the physical volume fraction distribution and the sharpness of the interface. The central differencing schemes are known to be unbounded for such a convection dominant flow as advection of the VOF function, while the UD schemes have the boundedness of the volume fraction. However, their solutions are diffusive over several CVs because the volume fraction is treated as a standard scalar field without a numerical strategy for maintaining the sharpness of the interface. On the other hand, the DD schemes are weak in preserving the boundedness without any specified conditions although they have a tendency to preserve the sharpness of the interface. In the interpolation of volume fractions from the cell centers to the cell faces, a downwind-like compressive differencing scheme is apt to provide a stair profile, a wrinkled interface, where the flow direction is almost perpendicular to the interface normal vector as reported by Hirt and Nichols [1] and Lafaurie *et al.* [25]. Therefore, a successful volume advection algorithm should combine the upwind and downwind schemes in a proper way to satisfy these two requirements. Most of the high resolution scheme-based VOF algorithms [1, 8, 23, 25, 28] couple a bounded downwind scheme with a bounded high-order upwind scheme or with the first-order upwind scheme using a blending function. It was realized that the accuracy of the methodology is strongly dependent on its blending strategy used to switch smoothly between the implemented differencing schemes [28]. The blending function must work continuously on the basis of the angle between the orientation of the interface and the flow direction.

The present VOF algorithm follows the above noted general approach and uses the similar high resolution schemes implemented in the HRIC, MHRIC, and CICSAM. In these methods the difference of the MHRIC with respect to the HRIC is that it combines the third-order ULTIMATE-QUICKEST [26] chosen by the CICSAM with the bounded downwind scheme derived in the HRIC. However, note that the present algorithm is developed on the basis of a different combination of high resolution schemes and a different blending function.

The high resolution schemes can be constructed with the aid of the normalized variable diagram (NVD) [26] and they are bounded by enforcing convection boundedness criteria (CBC) [37] for implicit and explicit flow calculations on their base interpolation profiles. The normalized volume fraction $\tilde{\alpha}$ for constructing a high resolution advection scheme is defined as

$$\tilde{\alpha}=\frac{\alpha-\alpha_{\mathrm{U}}}{\alpha_{\mathrm{A}}-\alpha_{\mathrm{U}}} \tag{14}$$

where the subscripts U and A denote the upwind and acceptor cells, respectively (see Figure 1). The center CV on whose cell faces interpolation of the volume fraction is performed is denoted as the donor cell D. For the case of non-uniform grids, the normalized cell face value is also a function of the normalized coordinates [38] given by $\tilde{\xi}_1=(\xi_1-\xi_{1\mathrm{U}})/(\xi_{1\mathrm{A}}-\xi_{1\mathrm{U}})$. However, for both uniform and non-uniform grids, the following differencing schemes, which are main components of the proposed VOF advection algorithm, use the same expressions: the first-order upwind scheme

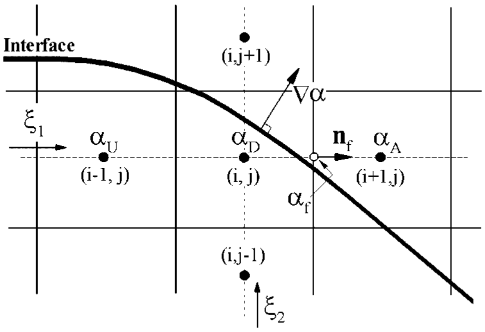

Figure 1. Definition of local variables for normalized variable diagram (NVD).

$\tilde{\alpha}_f = \tilde{\alpha}_D$, the downwind scheme $\tilde{\alpha}_f = 1$, and a high-order upwind scheme $\tilde{\alpha}_f = 2\tilde{\alpha}_D$. To preserve the interface sharpness, we consider a combination of CBC value, named as Hyper-C [26], which is the most compressive downwind scheme capable of reducing numerical diffusion errors [25] and given by

$$\tilde{\alpha}_{f\ (\text{Hyper-C})} = \begin{cases} \min\left(\dfrac{\tilde{\alpha}_D}{Co}, 1\right) & \text{where } 0 \leqslant \tilde{\alpha}_D \leqslant 1 \\ \tilde{\alpha}_D & \text{elsewhere} \end{cases} \tag{15}$$

where $\tilde{\alpha}_f$ is the normalized volume fraction at the cell face f and Co is the Courant number defined as

$$Co = \frac{\dot{m}_f \Delta t}{\Delta\Omega_D} \tag{16}$$

in which $\dot{m}_f$ is the total flux out of the cell face f, Δt is the timestep, and $\Delta\Omega_D$ is the total volume of the donor cell D. Instead of the ULTIMATE-QUICKEST scheme, which is used in the CICSAM for the boundedness of the volume fraction distribution, we propose a less complicated and lower-order scheme, $\tilde{\alpha}_f = 2\tilde{\alpha}_D$, that is one basis element of the HRIC's bounded DD scheme. After enforcing the CBC for explicit flow calculations blended with the Hyper-C scheme, the proposed high resolution scheme can be rewritten as

$$\tilde{\alpha}_{f\ (\text{HRIC})} = \begin{cases} \min(\tilde{\alpha}_D Co + 2\tilde{\alpha}_D(1-Co), \tilde{\alpha}_{f\ (\text{Hyper-C})}) & \text{where } 0 \leqslant \tilde{\alpha}_D \leqslant 1 \\ \tilde{\alpha}_D & \text{elsewhere} \end{cases} \tag{17}$$

To achieve the balance between the smoothness and sharpness of the interface, we need a blending function that switches gradually between the Hyper-C and our proposed high resolution scheme. For this, we implement the following weighting factor, which is based on the orientation of the interface and the flow direction:

$$\gamma_f = \cos^4(\theta_f) \tag{18}$$

where

$$\theta_f = \arccos\left|\frac{(\nabla\alpha)_f \cdot \mathbf{n}_f}{|(\nabla\alpha)_f|\,|\mathbf{n}_f|}\right| \tag{19}$$

Copyright © 2009 John Wiley & Sons, Ltd.

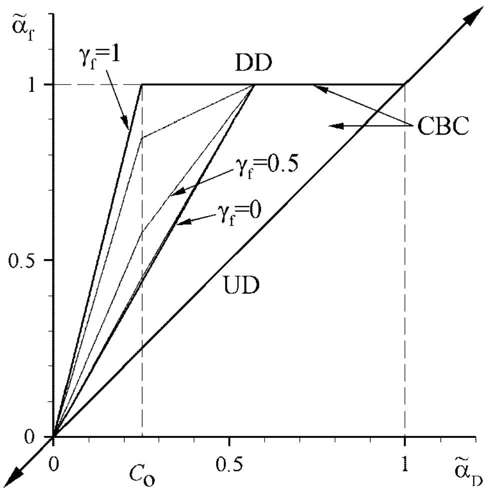

Figure 2. NDV for the present volume-of-fluid (VOF) advection algorithm. UD: upwind differencing, DD: downwind differencing, CBC: convection boundedness criteria.

and $\mathbf{n}_f$ is the vector connecting the centers of the CV D and A. We use a blending function of higher degree than that of the CICSAM, $\gamma_f = 0.5(\cos(2\theta_f)+1) = \cos^2(\theta_f)$ [28]. We found that the weighting function (18) is more suitable to our VOF method. Finally, the normalized cell face value for the volume fraction computed by using the proposed high resolution advection scheme is then given by

$$\tilde{\alpha}_f = \gamma_f \tilde{\alpha}_{f\ (\text{Hyper-C})} + (1-\gamma_f)\tilde{\alpha}_{f\ (\text{HRIC})} \tag{20}$$

The NDV for the present VOF algorithm is shown in Figure 2. In the numerical results section, we will demonstrate that the present method provides a nearly equivalent order of accuracy to the CICSAM and is superior to some other VOF groups including the original HRIC and the MHRIC.

2.3. Level-set distancing

It is well known that the VOF method is inaccurate when calculating the normal and curvature of the interface because of the discontinuous property in spatial derivatives of the volume fraction. In recent years, the CLSVOF methods [31–33] have been developed not only to satisfy mass conservation but also to maintain the accuracy of the normal and curvature calculations by retaining each good property. There are various implementation schemes to combine the level-set and the VOF methods. In the present free surface algorithm, we only consider the level-set distancing algorithm without advection of the level-set function and the succeeding re-distancing procedure. The present method couples the VOF and the level-set methods in a straightforward way. The level-set function ϕ is constructed at every timestep using the following hyperbolic level-set distancing equation [39] after solving the VOF advection equation:

$$\frac{\partial \phi}{\partial \tau} = \text{sign}(\phi_\alpha)(1-|\nabla\phi|) \tag{21}$$

Copyright © 2009 John Wiley & Sons, Ltd.

where τ is the artificial time. It is recommended to smooth the sign of the level-set function, $\mathrm{sign}(\phi_\alpha)$, for better conservation properties and more stable approximation. We use a version [39] based on a smoothed Heaviside function given by

$$\mathrm{sign}_\varepsilon(\phi_\alpha)=\begin{cases}-1 & \text{when } \phi_\alpha<\varepsilon\\ 2(H_\varepsilon(\phi_\alpha)-\frac{1}{2}) & \text{when } |\phi_\alpha|\leqslant\varepsilon\\ 1 & \text{when } \phi_\alpha>\varepsilon\end{cases} \tag{22}$$

where ε is the interface thickness in one fluid phase, which is proportional to the grid size Δh, and $H_\varepsilon(\phi_\alpha)$ is a smooth Heaviside function defined by

$$H_\varepsilon(\phi_\alpha)=\begin{cases}0 & \text{when } \phi_\alpha<\varepsilon\\ \dfrac{1}{2}\left(1+\dfrac{\phi_\alpha}{\varepsilon}+\dfrac{1}{\pi}\sin\left(\dfrac{\pi\phi_\alpha}{\varepsilon}\right)\right) & \text{when } |\phi_\alpha|\leqslant\varepsilon\\ 1 & \text{when } \phi_\alpha>\varepsilon\end{cases} \tag{23}$$

The variable ϕ_α is an initial level-set function whose zero-level-set is the interface. This initial function shares the same interface represented by the VOF function α, which can be derived as

$$\phi_\alpha=2\varepsilon(\alpha-0.5) \tag{24}$$

We set $\varepsilon=2\Delta h$ and solve the level-set distancing equation, (21), up to $\tau=2\varepsilon$ in order to let the level-set function ϕ have the signed-distance property at least in the region ε. The solution of ϕ might have a stair-like or saw-tooth profile of the interface because the initial function ϕ_α is constructed on the basis of the discontinuous VOF property. To remove the unexpected local instability, we use the 5-points Chebyshev filter function. It should be noted that this kind of additional smoothing process can be another source of mass loss. However, in the numerical results we found that the volume difference between the level-set and the VOF representations after this smoothing treatment satisfactorily decreases as grid resolution increases. In case on a two-dimensional equal spaced structured grid, the smoothing is performed as

$$\bar{\phi}_{\mathrm{D}}=0.5(\bar{\phi}_{\mathrm{D}\xi_1}+\bar{\phi}_{\mathrm{D}\xi_2}) \tag{25}$$

where $\bar{\phi}_{\mathrm{D}}$ is a smoothed level-set value at the cell center D, the subscripts ξ_1, ξ_2 denote the constant coordinates whose lines are grid lines as shown in Figure 1, and

$$\bar{\phi}_{\mathrm{D}\xi_1}=\tfrac{1}{16}(-\phi_{i-2,j}+4\phi_{i-1,j}+10\phi_{i,j}+4\phi_{i+1,j}-\phi_{i+2,j}) \tag{26}$$

$$\bar{\phi}_{\mathrm{D}\xi_2}=\tfrac{1}{16}(-\phi_{i,j-2}+4\phi_{i,j-1}+10\phi_{i,j}+4\phi_{i,j+1}-\phi_{i,j+2}) \tag{27}$$

This smoothing formula can be extended to variable grid spacing cases and various different types of filter function can be implemented for unstructured grid cases.

Copyright © 2009 John Wiley & Sons, Ltd.

3. NUMERICAL IMPLEMENTATIONS

3.1. Discretization of the Navier–Stokes equations

We use the cell-centered finite volume method based on a second-order implicit discretization to solve the governing equations as discussed in [40]. The discretization procedure will be shown for a two-dimensional case. However, the extension of the discretization to three-dimensional problems considering grids of any kind is straightforward [40]. The fluid domain is decomposed into a structured grid of quadrilateral CVs. A typical two-dimensional CV and the notation used for a two-dimensional grid are shown in Figure 3. The computational node is placed in the center of each CV at which all unknowns and all fluid properties are stored and the governing equations are applied, leading to a linearized algebraic equation.

We use a fully implicit time discretization of second-order accuracy, which is given by

$$\frac{\partial}{\partial t}\int_{\Omega}\rho u_i\,\mathrm{d}\Omega\approx\left(\rho\frac{\partial u_i}{\partial t}\right)_{\mathrm{P}}^{m}\Delta\Omega_{\mathrm{P}}\approx\left(\rho\frac{3u_i^m-4u_i^{m-1}+u_i^{m-2}}{2\Delta t}\right)_{\mathrm{P}}\Delta\Omega_{\mathrm{P}} \tag{28}$$

where the superscript m is the timestep counter and denotes the current time instant, while the superscripts $m-1$ and $m-2$ denote the previous two succeeding timesteps. We use an adaptive timestep control that determines the timestep Δt by the convective timestep restriction due to the local Courant number (16).

From the midpoint rule and the Picard iteration algorithm, the nonlinear convection term in the momentum equations can be linearized as

$$\int_S \rho u_i\mathbf{v}\cdot\mathbf{n}\,\mathrm{d}S\approx\sum_c \rho_c u_{ic}^m\left(u_{1c}^{m-1}S_c^{x_1}+u_{2c}^{m-1}S_c^{x_2}\right)=\sum_c u_{ic}^m\dot{m}_c^{m-1},\quad c=\mathrm{e},\mathrm{w},\mathrm{n},\mathrm{s} \tag{29}$$

where u_{ic}^m are the unknown velocity components at the cell faces c, u_{1c}^{m-1}, u_{2c}^{m-1} are the Cartesian velocity components from the previous time step, and $\dot{m}_c^{m-1}$ are the mass fluxes through the cell faces c. $S_c^{x_1}$, $S_c^{x_2}$ are the Cartesian components of the surface vector $(\mathbf{n}S)_c$, with surface area S. Note that the surface vector components are computed and stored only at the east and north faces

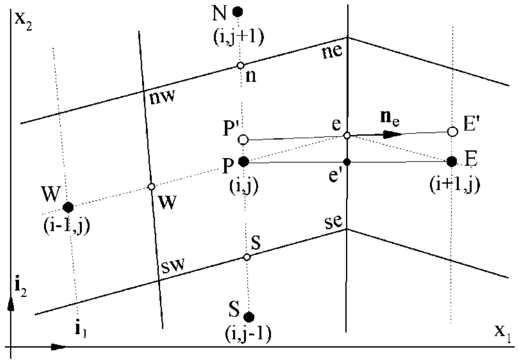

Figure 3. A two-dimensional control volume (CV) and the notation used.

Copyright © 2009 John Wiley & Sons, Ltd.

of the CV centered on a node because neighboring CVs around the node own their cell faces jointly with each other. The components of the surface vectors $(\mathbf{n}S)_\mathrm{e}$, $(\mathbf{n}S)_\mathrm{n}$ are defined as

$$S_\mathrm{e}^{x_1}=(x_{2\mathrm{ne}}-x_{2\mathrm{se}})r_\mathrm{e}, \quad S_\mathrm{e}^{x_2}=(x_{1\mathrm{se}}-x_{1\mathrm{ne}})r_\mathrm{e} \tag{30}$$

$$S_\mathrm{n}^{x_1}=(x_{2\mathrm{nw}}-x_{2\mathrm{ne}})r_\mathrm{n}, \quad S_\mathrm{n}^{x_2}=(x_{1\mathrm{ne}}-x_{1\mathrm{nw}})r_\mathrm{n} \tag{31}$$

where r_e and r_n are the distances of the cell face center e and n from the origin of the reference coordinate system, respectively. When $c=e$, the cell face velocity $u_{i\mathrm{e}}^{m-1}$ is approximated by using the following second-order symmetric formula:

$$u_{i\mathrm{e}}^{m-1}=(u_{i\mathrm{P}}^{m-1}+(\nabla u_i^{m-1})_\mathrm{P}\cdot(\mathbf{r}_{\mathrm{P}'}-\mathbf{r}_\mathrm{P}))\lambda_{\mathrm{e,P}}+(u_{i\mathrm{E}}^{m-1}+(\nabla u_i^{m-1})_\mathrm{E}\cdot(\mathbf{r}_{\mathrm{E}'}-\mathbf{r}_\mathrm{E}))(1-\lambda_{\mathrm{e,P}}) \tag{32}$$

in which $\lambda_{\mathrm{e,P}}$ is the interpolation factor defined by the position vectors of the cell face centers and expressed as

$$\lambda_{\mathrm{e,P}}=\frac{|\mathbf{r}_\mathrm{e}-\mathbf{r}_\mathrm{P}|}{|\mathbf{r}_\mathrm{e}-\mathbf{r}_\mathrm{P}|+|\mathbf{r}_\mathrm{E}-\mathbf{r}_\mathrm{e}|} \tag{33}$$

The gradient of velocity $(\nabla u_i^{m-1})_\mathrm{P}$ in (32) is explicitly calculated with the aid of the Gauss' divergence theorem as

$$(\nabla u_i^{m-1})_\mathrm{P}\approx\frac{\int_{\Omega_\mathrm{P}}\nabla u_i^{m-1}\,\mathrm{d}\Omega}{\Delta\Omega_\mathrm{P}}=\frac{\int_{S_c}u_i^{m-1}\mathbf{i}_i\cdot\mathbf{n}\,\mathrm{d}S}{\Delta\Omega_\mathrm{P}}\approx\frac{\sum_c u_{ic}^{m-1}\mathbf{n}_c S_c}{\Delta\Omega_\mathrm{P}}, \quad c=\mathrm{e,w,n,s} \tag{34}$$

where u_{ic}^{m-1} are calculated in the same way as (32), but several iterations between (32) and (34) are necessary for convergence. When $c=e$, the unknown convective variable $u_{i\mathrm{e}}^m$ is calculated by using the differed correction scheme [41] blending of the first-order UD with a third-order monotone upstream-centered schemes for conservation laws (MUSCL) [42] as

$$u_{i\mathrm{e}}^m=u_{i\mathrm{e}}^{m,\mathrm{UD}}+\lambda_{u_i}(u_{i\mathrm{e}}^{m-1,\mathrm{UD}}-u_{i\mathrm{e}}^{m-1,\mathrm{MUSCL}}) \tag{35}$$

where λ_{u_i} is the blending factor with $0\leqslant\lambda_{u_i}\leqslant 1$. This factor is set to unity in the present study. Finally the convective terms (29) are constructed as

$$\begin{aligned}\dot{m}_\mathrm{e}^{m-1}u_{i\mathrm{e}}^m\approx{}&\min(\dot{m}_\mathrm{e}^{m-1},0)u_{i\mathrm{E}}^m+\max(\dot{m}_\mathrm{e}^{m-1},0)u_{i\mathrm{P}}^m\\&+\lambda_{u_i}(\min(\dot{m}_\mathrm{e}^{m-1},0)u_{i\mathrm{E}}^{m-1}+\max(\dot{m}_\mathrm{e}^{m-1},0)u_{i\mathrm{P}}^{m-1}-u_{i\mathrm{e}}^{m-1,\mathrm{MUSCL}})\end{aligned} \tag{36}$$

where

$$u_{i\mathrm{e}}^{m-1,\mathrm{MUSCL}}=\left\{\begin{array}{l}u_{i\mathrm{E}}^{m-1}+(\lambda_3+\lambda_4)\,\mathrm{sign}(1,\Delta u_{i\mathrm{E}}^{m-1})\max(0,\min(|\Delta u_{i\mathrm{E}}^{m-1}|,\Delta u_{i\mathrm{P}}^{m-1}\,\mathrm{sign}(1,\Delta u_{i\mathrm{E}}^{m-1})))\\ \quad\text{when } \dot{m}_\mathrm{e}^{m-1}<0\\ u_{i\mathrm{P}}^{m-1}+(\lambda_1+\lambda_2)\,\mathrm{sign}(1,\Delta u_{i\mathrm{W}}^{m-1})\max(0,\min(|\Delta u_{i\mathrm{W}}^{m-1}|,\Delta u_{i\mathrm{P}}^{m-1}\,\mathrm{sign}(1,\Delta u_{i\mathrm{W}}^{m-1})))\\ \quad\text{when } \dot{m}_\mathrm{e}^{m-1}\geqslant 0\end{array}\right\} \tag{37}$$

Copyright © 2009 John Wiley & Sons, Ltd.

with

$$\begin{aligned}\lambda_1 &= \frac{(2-\lambda_{e,W})\lambda_{e,P}^2}{1+\lambda_{e,P}-\lambda_{e,W}}, \quad \lambda_2=\frac{(1-\lambda_{e,P})(1-\lambda_{e,W})^2}{1+\lambda_{e,P}-\lambda_{e,W}}\\ \lambda_3 &= \frac{(1+\lambda_{e,W})(1-\lambda_{e,P})^2}{1+\lambda_{e,E}-\lambda_{e,P}}, \quad \lambda_4=\frac{\lambda_{e,P}\lambda_{e,E}^2}{1+\lambda_{e,E}-\lambda_{e,P}}\end{aligned} \tag{38}$$

$$\Delta u_{iW}^{m-1}=u_{iP}^{m-1}-u_{iW}^{m-1}, \quad \Delta u_{iP}^{m-1}=u_{iE}^{m-1}-u_{iP}^{m-1}, \quad \Delta u_{iE}^{m-1}=u_{iEE}^{m-1}-u_{iE}^{m-1} \tag{39}$$

in which the subscript EE denotes the acceptor cell of the CV E. The implicit terms in the discretized convective terms construct the elements of the coefficients matrix and the explicit higher-order terms are added to the source term of the linearized equation system.

The diffusive terms of (2) can be approximated as

$$\begin{aligned}\int_S \tau_{ij}\mathbf{i}_j\cdot\mathbf{n}\,\mathrm{d}S &\approx \sum_c S_c\mu_c\left(\mathrm{grad}(u_i^m)\cdot\mathbf{n}+\left(\frac{\partial u_j^{m-1}}{\partial x_i}\right)\mathbf{i}_j\cdot\mathbf{n}\right)_c\\ &=\sum_c S_c\mu_c\left(\left(\frac{\partial u_i^m}{\partial n}\right)+\left(\frac{\partial u_j^{m-1}}{\partial x_i}\right)\mathbf{i}_j\cdot\mathbf{n}\right)_c, \quad c=\mathrm{e,w,n,s}\end{aligned} \tag{40}$$

Although the sum of the second term in the brackets is zero when the density and the viscosity of the fluid are constant, we explicitly include this discretized term as one of the source terms in the equation system. In order to prevent unphysical oscillatory solutions the first term on the right-hand side of (40) can be approximated in a deffered correction manner suggested by Muzaferija [43] and given by

$$\left(\frac{\partial u_i^m}{\partial n}\right)_e \approx \frac{u_{iE}^m-u_{iP}^m}{|\mathbf{r}_E-\mathbf{r}_P|}+(\mathrm{grad}\,u_i^{m-1})_e\cdot\left(\mathbf{n}_e-\frac{\mathbf{r}_E-\mathbf{r}_P}{|\mathbf{r}_E-\mathbf{r}_P|}\right) \tag{41}$$

The first term on the right-hand side is an implicit diffusion flux approximation and follows the usual central differencing scheme of second-order accuracy on a Cartesian grid. The second term considers the difference between the gradients in the normal $\mathbf{n}_e$ and grid line ξ_e directions, which makes the convergence behavior be of second-order accuracy even on a non-orthogonal grid.

The volumetric sources terms, body force terms, are calculated by using midpoint rule as

$$\int_\Omega f_{\sigma i}\,\mathrm{d}\Omega+\int_\Omega \rho g_i\,\mathrm{d}\Omega\approx(f_{\sigma i}+\rho g_i)_P^{m-1}\Delta\Omega_P \tag{42}$$

The pressure terms are approximated as body forces and given by

$$-\int_S p\mathbf{i}_i\cdot\mathbf{n}\,\mathrm{d}S=-\int_\Omega(\mathrm{grad}\,p\cdot\mathbf{i}_i)\,\mathrm{d}\Omega\approx-(\mathrm{grad}\,p\cdot\mathbf{i}_i)_P^{m-1}\Delta\Omega_P \tag{43}$$

This approach is conservative because we calculate the derivatives of the pressure by using the Gauss' divergence theorem as (34).

Copyright © 2009 John Wiley & Sons, Ltd.

Finally, an algebraic equation is obtained by summing up all discretized cell face fluxes and volume integrals for each CV and expressed as

$$A_{\mathrm{P}} u_{i\mathrm{P}}^{m} + \sum_{l} A_{l} u_{il}^{m} = Q_{\mathrm{P}}, \quad l = \mathrm{E, W, N, S} \tag{44}$$

where the coefficients A_l contain the contributions of the unknown terms in the convection and diffusion fluxes and Q_{P} includes all the source terms, explicitly calculated surface integrals and the unsteady term. The constructed algebraic equations are solved by using the Stone's solver [44] based on incomplete LU decomposition.

3.2. Pressure–velocity coupling

The velocity components computed from the momentum equations do not satisfy the continuity equation. To achieve divergence-free velocity field, we use the SIMPLE algorithm [45]. Since the collocated variable arrangement is chosen, the artificial dissipation term in pressure correction equation is added to detect oscillations and smooth them out, as discussed in [40]. The cell face normal velocity can be corrected by considering the difference between the pressure gradient and the interpolated gradient at cell faces and given for the cell face e by

$$\left(\frac{\partial u_i^{m*}}{\partial n}\right)_{\mathrm{e}} = \overline{\left(\frac{\partial u_i^{m*}}{\partial n}\right)_{\mathrm{e}}} - \left(\overline{\frac{\Delta\Omega}{A_{\mathrm{P}}}}\right)_{\mathrm{e}} \left(\frac{p_{\mathrm{E}} - p_{\mathrm{P}}}{(\mathbf{r}_{\mathrm{E}} - \mathbf{r}_{\mathrm{P}}) \cdot \mathbf{n}} - \frac{\overline{\operatorname{grad} p} \cdot (\mathbf{r}_{\mathrm{E}} - \mathbf{r}_{\mathrm{P}})}{(\mathbf{r}_{\mathrm{E}} - \mathbf{r}_{\mathrm{P}}) \cdot \mathbf{n}}\right)^{m-1} \tag{45}$$

where the superscript $*$ denotes the solution satisfying the momentum equation at the so-called predictor stage and the over-bar terms are spatially interpolated from neighbor nodal values. Using this approximation, the rate of change for the mass flux is calculated and modified to satisfy the continuity requirement by adding a correction term, $\Delta\dot{m}'$, and can be written as

$$\sum_{c} \dot{m}_c^{m*} + \Delta\dot{m}'_c = \sum_{c} \left(\frac{\partial u_i^{m*}}{\partial n} + \frac{\partial u'_i}{\partial n}\right)_c = 0, \quad c = \mathrm{e, w, n, s} \tag{46}$$

where the second term on the right-hand side is the correction term expressed by the velocity correction, which is given by

$$\left(\frac{\partial u'_i}{\partial n}\right)_{\mathrm{e}} \approx \left(\overline{\frac{\Delta\Omega}{A_{\mathrm{P}}}}\right)_{\mathrm{e}} \frac{p'_{\mathrm{E}} - p'_{\mathrm{P}}}{|\mathbf{r}_{\mathrm{E}} - \mathbf{r}_{\mathrm{P}}|} \tag{47}$$

From the correction equation for the mass flux, a discrete form of the Poisson equation for pressure correction p' can be obtained and its algebraic equation is then given by

$$A_{p\mathrm{P}} p'_{\mathrm{P}} + \sum_{l} A_{pl} p'_l = -Q_m^*, \quad l = \mathrm{E, W, N, S} \tag{48}$$

where the coefficients A_{pl} contain contributions of convection-like and diffusion-like terms and the term Q_m^* is the mass imbalance on the right-hand side of (46). After obtaining the field of pressure correction p', velocity and pressure are corrected, respectively, as

$$u_i^m = u_i^{m*} + u'_i \approx u_i^{m*} - \frac{1}{A_{\mathrm{P}}} \sum_{c} p' S_c, \quad c = \mathrm{e, w, n, s} \tag{49}$$

$$p^m = p^{m-1} + p' \tag{50}$$

Copyright © 2009 John Wiley & Sons, Ltd.

DOI: 10.1002/fld

3.3. Discretization of the VOF and the level-set distancing equations

The convection term in (6) can be approximated in a similar way employed in the discretization of the momentum equations. However, note that the interpolation of the VOF values at the cell faces should be carried out differently from that for other general scalar fields as demonstrated in Section 2.2. From the midpoint integral rule, the convection term of the VOF equation is expressed as

$$\int_S \alpha \mathbf{v}\cdot\mathbf{n}\,\mathrm{d}S \approx \sum_c \alpha_c^m \dot{m}_c^m, \quad c=\mathrm{e,w,n,s} \tag{51}$$

For spatial discretization, the normalized volume fraction at a cell face needs to be restored to its actual value through the manipulation of the NVD formulation. Upon the previously constructed high resolution advection algorithm, the unknown volume fraction value at the cell face e is calculated as

$$\alpha_\mathrm{e}^m = \alpha_\mathrm{P}^m(1-\beta_\mathrm{e}) + \alpha_\mathrm{E}^m \beta_\mathrm{e} \tag{52}$$

where

$$\beta_\mathrm{e} = \frac{\tilde{\alpha}_\mathrm{e} - \tilde{\alpha}_\mathrm{P}}{1-\tilde{\alpha}_\mathrm{P}} \tag{53}$$

We use the second-order Crank–Nicolson scheme to discretize the time integral of (6), which leads the VOF equation to the following fully implicit approximation:

$$\alpha_\mathrm{P}^m \frac{\Delta\Omega_\mathrm{P}}{\Delta t} + \sum_c \frac{1}{2}\alpha_c^m \dot{m}_c^m = \alpha_\mathrm{P}^{m-1}\frac{\Delta\Omega_\mathrm{P}}{\Delta t} - \sum_c \frac{1}{2}\alpha_c^{m-1}\dot{m}_c^m, \quad c=\mathrm{e,w,n,s} \tag{54}$$

By summing up the temporal and surface integral terms, an algebraic equation is obtained that connects the volume factions at each CV center with those at its adjacent central nodes.

The level-set distancing equation (21) is explicitly solved by using the first-order explicit Euler scheme in time and a fifth-order weighted essentially non-oscillatory (WENO) scheme [46] in space. In [47], it is noted that the fifth-order WENO scheme shows a superior performance than other ENO schemes, leading to a good mass conservation with the compressive interface. The discretized level-set distancing equation at a CV center P is given by

$$\phi_\mathrm{P}^\tau = \phi_\mathrm{P}^{\tau-\Delta\tau} + \mathrm{sign}(\phi_\alpha^{\tau=0})\Delta\tau\left(1-\sqrt{\phi_{x_1}^2+\phi_{x_2}^2}\right)_\mathrm{P}^{\tau-\Delta\tau} \tag{55}$$

where the derivatives ϕ_{x_j} are obtained through the upwind procedure [39] as

$$\phi_{x_j} \approx \left\{\begin{array}{ll} \phi_{x_j}^+ & \text{where } \phi_{x_j}^+\,\mathrm{sign}(\phi_\alpha)<0 \text{ and } \phi_{x_j}^-\,\mathrm{sign}(\phi_\alpha)<-\phi_{x_j}^+\,\mathrm{sign}(\phi_\alpha) \\ \phi_{x_j}^- & \text{where } \phi_{x_j}^-\,\mathrm{sign}(\phi_\alpha)>0 \text{ and } \phi_{x_j}^+\,\mathrm{sign}(\phi_\alpha)>-\phi_{x_j}^-\,\mathrm{sign}(\phi_\alpha) \\ \frac{1}{2}(\phi_{x_j}^+ + \phi_{x_j}^-) & \text{elsewhere} \end{array}\right\} \tag{56}$$

where $\phi_{x_j}^+$ and $\phi_{x_j}^-$ denote the right-biased and left-biased differencings, respectively. These derivatives can be calculated by using the fifth-order WENO scheme as

$$\phi_{x_1}^\pm = \omega_1^\pm\left(\frac{d_1^\pm}{3} - \frac{7d_2^\pm}{6} + \frac{11d_3^\pm}{6}\right) + \omega_2^\pm\left(-\frac{d_2^\pm}{6} + \frac{5d_3^\pm}{6} + \frac{d_4^\pm}{3}\right) + \omega_3^\pm\left(\frac{d_3^\pm}{3} + \frac{5d_4^\pm}{6} - \frac{d_5^\pm}{6}\right) \tag{57}$$

Copyright © 2009 John Wiley & Sons, Ltd.

DOI: 10.1002/fld

with

$$
\begin{aligned}
&d_1^+ = \frac{\phi_{i+3,j}-\phi_{i+2,j}}{\Delta\xi_1}, \quad d_2^+ = \frac{\phi_{i+2,j}-\phi_{i+1,j}}{\Delta\xi_1}, \quad d_3^+ = \frac{\phi_{i+1,j}-\phi_{i,j}}{\Delta\xi_1}\\
&d_4^+ = \frac{\phi_{i,j}-\phi_{i-1,j}}{\Delta\xi_1}, \quad d_5^+ = \frac{\phi_{i-1,j}-\phi_{i-2,j}}{\Delta\xi_1}
\end{aligned}
\tag{58}
$$

$$
\begin{aligned}
&d_1^- = \frac{\phi_{i-2,j}-\phi_{i-3,j}}{\Delta\xi_1}, \quad d_2^- = \frac{\phi_{i-1,j}-\phi_{i-2,j}}{\Delta\xi_1}, \quad d_3^- = \frac{\phi_{i,j}-\phi_{i-1,j}}{\Delta\xi_1}\\
&d_4^- = \frac{\phi_{i+1,j}-\phi_{i,j}}{\Delta\xi_1}, \quad d_5^- = \frac{\phi_{i+2,j}-\phi_{i+1,j}}{\Delta\xi_1}
\end{aligned}
\tag{59}
$$

The respective weights $\omega^\pm$ are given by

$$
\omega_1^\pm = \frac{\varpi_1^\pm}{\varpi_1^\pm+\varpi_2^\pm+\varpi_3^\pm}, \quad \omega_2^\pm = \frac{\varpi_2^\pm}{\varpi_1^\pm+\varpi_2^\pm+\varpi_3^\pm}, \quad \omega_3^\pm = \frac{\varpi_3^\pm}{\varpi_1^\pm+\varpi_2^\pm+\varpi_3^\pm}
\tag{60}
$$

with

$$
\varpi_1^\pm = \frac{1}{10(\tilde{\varepsilon}+\mathrm{IS}_1^\pm)^2}, \quad \varpi_2^\pm = \frac{6}{10(\tilde{\varepsilon}+\mathrm{IS}_2^\pm)^2}, \quad \varpi_3^\pm = \frac{3}{10(\tilde{\varepsilon}+\mathrm{IS}_3^\pm)^2}
\tag{61}
$$

Here, $\tilde{\varepsilon}$ is a regularization parameter set to 10^{-6} and $\mathrm{IS}^\pm$ are the WENO smoothness indicators defined as

$$
\begin{aligned}
\mathrm{IS}_1^\pm &= \tfrac{13}{12}(d_1^\pm-2d_2^\pm+d_3^\pm)^2+\tfrac{1}{4}(d_1^\pm-4d_2^\pm+3d_3^\pm)^2\\
\mathrm{IS}_2^\pm &= \tfrac{13}{12}(d_2^\pm-2d_3^\pm+d_4^\pm)^2+\tfrac{1}{4}(d_2^\pm-d_4^\pm)^2\\
\mathrm{IS}_3^\pm &= \tfrac{13}{12}(d_3^\pm-2d_4^\pm+d_5^\pm)^2+\tfrac{1}{4}(3d_3^\pm-4d_4^\pm+d_5^\pm)^2
\end{aligned}
\tag{62}
$$

4. NUMERICAL RESULTS

4.1. Advection of interfaces

To measure the performance of the proposed VOF advection algorithm, we carried out two-dimensional advection tests with rigid interfaces of different shapes: translation tests of Rudman's shapes [22] and the rigid rotation of Zalesak's slotted disk [29]. We compared the accuracy of our solutions against those of other VOF algorithms, including the original HRIC and MHRIC schemes, which are implemented in our code for comparison.

4.1.1. Translations of hollow interfaces. For this validation test, we considered three interface shapes taken from [22]: a hollow square parallel to the coordinate axis, a hollow square rotated at 26.57° to the axis, and a hollow circle. The external width of the hollow square is 0.8 m and the internal width is 0.4 m. In the case of the hollow circle, its external and internal diameters have the dimensions corresponding to each square's width, respectively. The interface shapes are translated in a given oblique velocity field of (2, 1). The computational domain whose origin is at

Copyright © 2009 John Wiley & Sons, Ltd.

DOI: 10.1002/fld

Table I. Error results for the advection tests with an unidirectional velocity field.

Advection algorithm	Square	Rotated square	Circle
SLIC*	1.32E−01	1.08E−01	9.18E−02
Hirt.Nichols*	6.86E−03	1.60E−01	1.90E−01
FCT.VOF*	1.63E−08	8.15E−02	3.99E−02
Youngs*	2.58E−02	3.16E−02	2.98E−02
Stream/Youngs†	2.70E−02	3.08E−02	2.66E−02
Stream/Puckett†	3.33E−02	3.15E−02	6.96E−03
CICSAM-S‡	2.50E−02	4.00E−02	4.33E−02
CICSAM-U‡	3.97E−02	4.00E−02	2.84E−02
HRIC	8.64E−02	1.22E−01	1.08E−01
MHRIC	7.74E−02	9.90E−02	9.19E−02
Proposed method	1.91E−02	4.63E−02	4.03E−02

*,†,‡Errors obtained from References [18, 22, 28], respectively.

(0, 0) is $4\times 4\,\mathrm{m}^2$ and composed of 200×200 uniformly spaced structured grid cells. The centers of the shapes are initially placed at (0.75, 0.75), and the final new centers are theoretically at (3.25, 2.00) after 500 computational timesteps, which are determined on the basis of a Courant number of 0.25. The numerical errors for each test case are calculated as follows:

$$E=\frac{\sum_i^{\text{all cells}}|\alpha_i^m-\alpha_i^a|}{\sum_i^{\text{all cells}}\alpha_i^0} \tag{63}$$

where α^m is the VOF function at the end of the advection, α^a is the analytic VOF function, and α^0 is the initial VOF function. Table I compares our numerical errors with those of other VOF algorithms reported in [18, 22, 28]. The final shapes are compared with the initial conditions in Figure 4 in which the three contour intervals of the volume fractions are 0.025, 0.5, and 0.975, respectively. Although we use a simple order scheme, a basis of the original HRIC scheme, lower than the third-order ULTIMATE-QUICKEST used by the CICSAM and also by the MHRIC, our method provides an improved accuracy over the two HRIC methods. The present results, inclusive of those of the CICSAM, are more comparable in accuracy to Youngs' and Stream's geometric interface reconstruction-based algorithms of higher accuracy than other VOF methods listed in Table I.

4.1.2. Rotation of slotted circle. As a translation case, this test also considers an interface of a slotted disk shape in a given velocity field and compares the final shape and position with those of the analytic solution. The computational domain has the same dimensions and grid cells as those used in the previous translation test. The circular disk has a diameter of 1.0 m and is cut by a slot of 0.12 m in width and 0.6 m in height. The disk has its center at (2.0, 2.75) and is driven to rotate by a circular flow of angular velocity 0.5 rad/s centered at (2.0, 2.0). The total computational timestep for one complete revolution of the disk is 2524, which corresponds to a Courant number of 0.25. In Figure 5, we compare the final shape after one complete revolution with the initial shape. In Table II, we provide our numerical error with those reported in [18, 22, 28]. As shown in the translation tests, the present VOF algorithm provides an accuracy close to Youngs' and Stream's algorithms as the CICSAM.

Copyright © 2009 John Wiley & Sons, Ltd.

DOI: 10.1002/fld

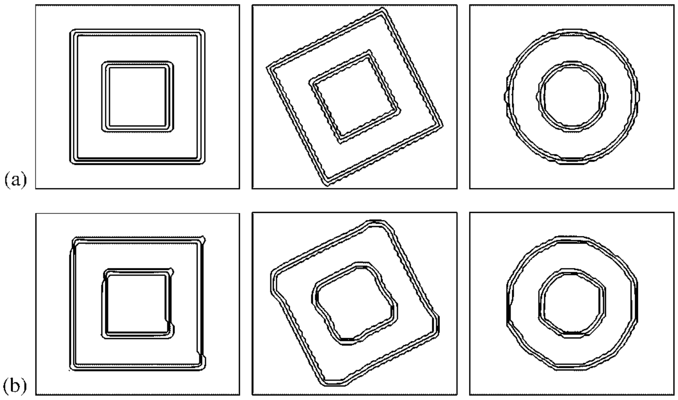

Figure 4. Advection with an unidirectional velocity field: (a) the initial conditions and (b) the final shapes for the proposed VOF scheme. Contours of the volume fraction are plotted at $\alpha=0.025$, $\alpha=0.5$, and $\alpha=0.975$.

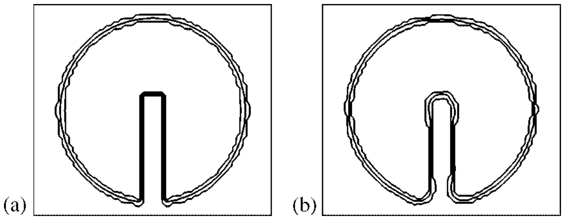

Figure 5. Zalesak's test for solid body rotation of a slotted circle: (a) the initial condition and (b) the final shape after one complete revolution for the proposed VOF scheme. Contours of the volume fraction are plotted at $\alpha=0.025$, $\alpha=0.5$, and $\alpha=0.975$.

Table II. Error results for the solid body rotation of a slotted circle.

Advection algorithm	Slotted circle
SLIC*	8.38E−02
Hirt.Nichols*	9.62E−02
FCT.VOF*	3.29E−02
Youngs*	1.09E−02
Stream/Youngs†	1.07E−02
Stream/Puckett†	1.00E−02
CICSAM-S‡	1.62E−02
CICSAM-U‡	2.02E−02
HRIC	6.86E−02
MHRIC	5.28E−02
Proposed method	1.77E−02

*,†,‡Errors obtained from References [18, 22, 28], respectively.

Copyright © 2009 John Wiley & Sons, Ltd.

Table III. Convergence study for an air bubble rising in viscous liquid: a spherical cap bubble. $\sigma = 0.007\,\mathrm{N/m}$, $Eo = 35.7$, $Mo = 3 \times 10^{-4}$.

Grid	E_{D_x}	E_{D_z}
$35 \times 35 \times 70$	N/A	N/A
$50 \times 50 \times 100$	0.00702	0.00599
$70 \times 70 \times 140$	0.00427	0.00265

4.2. *Air bubble rising in viscous flow*

As a validation of the present hybrid algorithm for surface tension problems, we have computed bubble motions with a large density ratio (1000:1) in three-dimensions. For comparison, we use computational results obtained by two different front tracking methods found in [48, 49]. As in [48], we consider two types of air bubbles in viscous liquids: a spherical cap bubble and an ellipsoidal bubble. We use the following dimensionless numbers to describe computational results: the Eötvös number and the Morton number, which are defined as

$$Eo = \frac{\rho_l g D_i^2}{\sigma}, \quad Mo = \frac{g \mu_l^4}{\rho_l \sigma^3} \tag{64}$$

where ρ_l is the liquid density, g is the acceleration of gravity, D_i is the initial bubble diameter, σ is the surface tension, and μ_l is the liquid viscosity. The initial diameter of an air bubble, $D_i = 5\,\mathrm{mm}$, is the same for both test cases. Except for the difference in surface tension, both cases use the same physical properties for each liquid: liquid density $\rho_l = 1000\,\mathrm{kg/m^3}$, viscosity $\mu_l = 0.01\,\mathrm{kg/(ms)}$, and $g = 9.8\,\mathrm{m/s^2}$. For the first case of a spherical cap bubble, we use a surface tension, $\sigma = 0.007\,\mathrm{N/m}$, and the corresponding two dimensionless numbers are $Eo = 35.7$ and $Mo = 3 \times 10^{-4}$. The dimensions of the computational domain are $1 \times 1 \times 2$. Free-slip conditions are given at the surrounding lateral surfaces and outflow conditions at the top of the domain. We made three consecutive grids with a refinement ratio of $\sqrt{2}$ for a grid convergence study: a coarse grid ($35 \times 35 \times 70$), a medium grid ($50 \times 50 \times 100$), and a fine grid ($70 \times 70 \times 140$). To compare with other numerical solutions, we measured the horizontal and vertical diameters of the rising bubble versus time as in [48]. In Table III, we provide the present grid convergence by the relative errors between two succeeding grids for the measured diameters (x_D, z_D) for the time duration $0 \leqslant t \leqslant 0.4$ in which these errors are calculated as

$$E_{Dx} = \frac{1}{t_{\max}} \sum_{t=0}^{t_{\max}} \left| \frac{x_{D1} - x_{D2}}{D_i} \right| \Delta t, \quad E_{Dz} = \frac{1}{t_{\max}} \sum_{t=0}^{t_{\max}} \left| \frac{z_{D1} - z_{D2}}{D_i} \right| \Delta t \tag{65}$$

where the additional subscripts 1 and 2 denote the solutions for the two succeeding grids, respectively. In Figure 6, the measured diameters versus time for three consecutive grids are compared with other numerical results reported in [48]. The results of our hybrid algorithm are in good agreement with those of the two front-tracking methods. This is expected since the surface tension-oriented errors are relatively small among these three methods for this test.

For the ellipsoidal bubble motion, we use surface tension, $\sigma = 0.07\,\mathrm{N/m}$, one order greater than that used for the previous spherical cap bubble calculation. The corresponding dimensionless numbers are then $Eo = 3.57$ and $Mo = 3 \times 10^{-7}$. In Table IV, we display the relative errors for the

Copyright © 2009 John Wiley & Sons, Ltd.

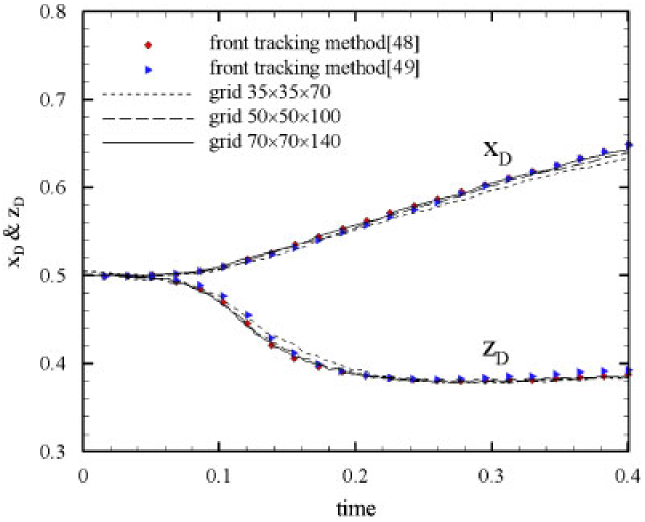

Figure 6. Comparison of the horizontal and vertical bubble dimensions as computed by the present hybrid method and two front-tracking methods found in [48, 49] for a spherical cap bubble.

Table IV. Convergence study for an air bubble rising in viscous liquid: an ellipsoidal bubble. $\sigma = 0.07\,\mathrm{N/m}$, $Eo = 3.57$, $Mo = 3\times 10^{-7}$.

Grid	E_{D_x}	E_{D_z}
$35\times 35\times 70$	N/A	N/A
$50\times 50\times 100$	0.01319	0.01322
$70\times 70\times 140$	0.00642	0.00884

transient diameters of the ellipsoidal bubbles computed for the same grid resolutions of the previous test. In Figure 7, we show the measured diameters of the bubble shape versus time in which the present algorithm provides a result comparable with those of the two front tracking methods as in the previous example, except that the differences increase in each horizontal diameter after the dimensionless time $t \approx 0.3$. The differences between the results of the three methods shown in Figure 7 are mainly caused by the differences of each algorithm for the surface tension correction and grid or surface mesh resolutions.

In Figure 8, we compare the discontinuous interface profiles from the volume fraction of $\alpha = 0.5$ with the level-set contours constructed at each final timestep of both simulations. In Table V, we show the volume difference in percent between the level-set and the VOF representations for the three consecutive grids computed after the level-set distancing process at the final timesteps of both bubble simulations. The expected small difference is provided by using our level-set distancing algorithm as the grid resolution increases. In Figure 9, we show the final bubble shapes at the two test conditions in which the figure on the right shows the ellipsoidal bubble with the pressure distribution.

Copyright © 2009 John Wiley & Sons, Ltd.

DOI: 10.1002/fld

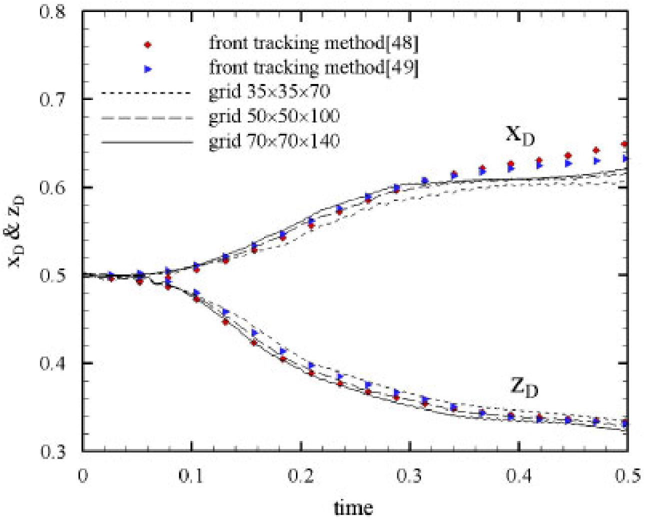

Figure 7. Comparison of the horizontal and vertical bubble dimensions as computed by the present hybrid method and two front-tracking methods found in [48, 49] for an ellipsoidal bubble.

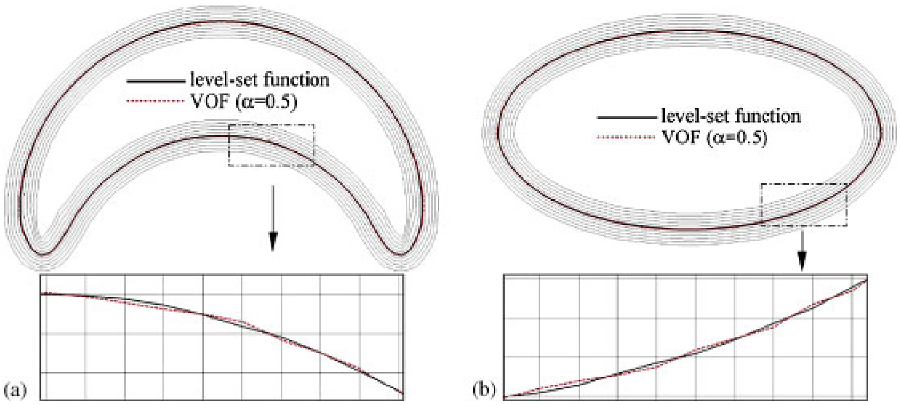

Figure 8. Level-set function constructed from the volume fraction of $\alpha = 0.5$ at the end of simulation: (a) a spherical cap bubble case at $t = 0.4$ and (b) an ellipsoidal bubble case at $t = 0.5$. Grid resolution is $70 \times 70 \times 140$.

4.3. Two-dimensional dam-break

As another way of validating the proposed free surface method, we have applied our VOF advection algorithm to more violent free surface flows interacting with a fixed structure: a dam-break following the experimental conditions found in [50]. It is well known that there is a typical benchmark test case [51] for dam-break problem in the literature that has different flow conditions from [50]. Up to now, various numerical methods: VOF method [1], front tracking-based MAC method [52], moving

Table V. Convergence study: volume difference in percent between the level-set and the VOF representations at the end of simulation.

Grid	Spherical cap bubble (%)	Ellipsoidal bubble (%)
35 × 35 × 70	0.635	0.399
50 × 50 × 100	0.524	0.249
70 × 70 × 140	0.194	0.114

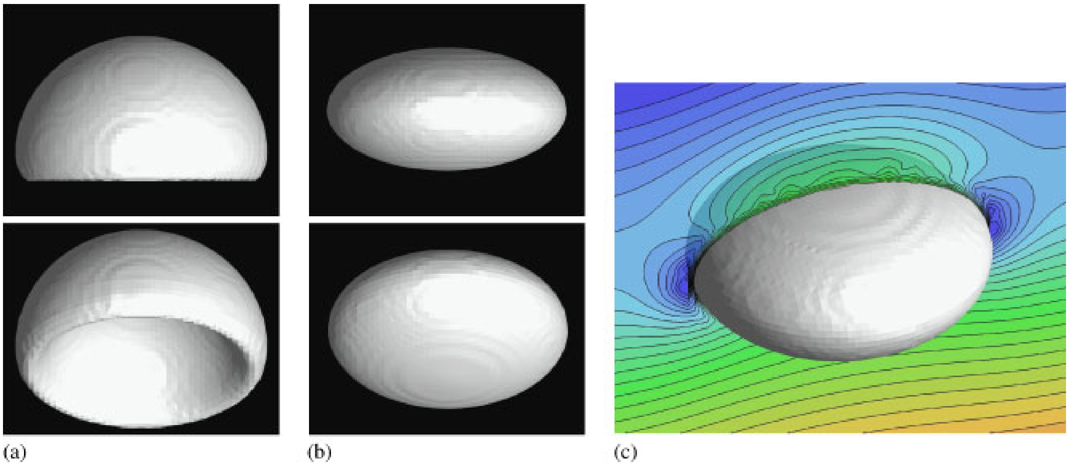

Figure 9. Three-dimensional shapes of a rising air bubble in liquid: (a) a spherical cap bubble (upper: side, lower: bottom) at $t=0.4$; (b) an ellipsoidal bubble (upper: side, lower: bottom) at $t=0.5$; and (c) the pressure field around the ellipsoidal bubble at $t=0.5$. Grid resolution is 70 × 70 × 140.

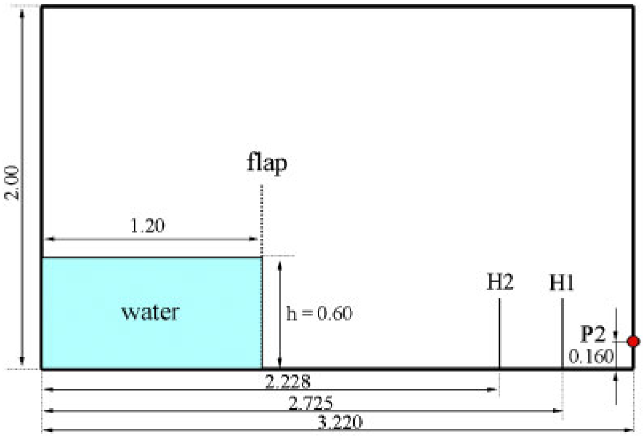

Figure 10. A two-dimensional dam-break: problem definition and measurement points for water heights and pressure.

Copyright © 2009 John Wiley & Sons, Ltd.

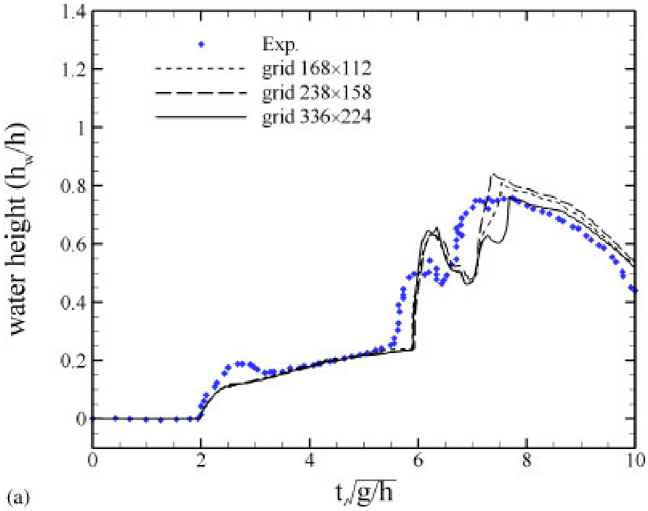

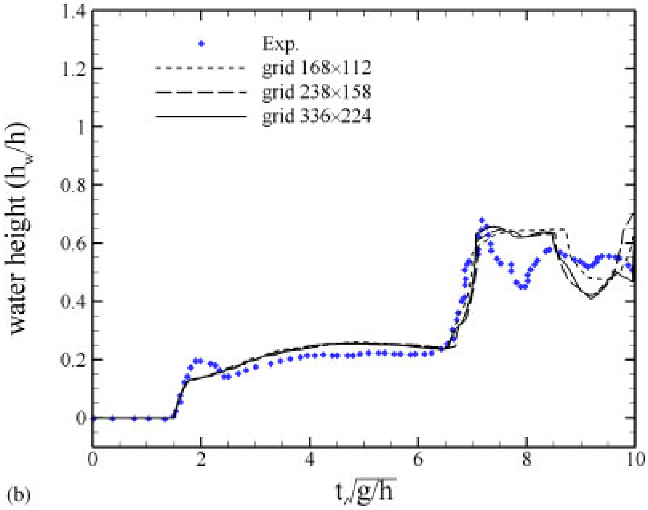

Figure 11. Vertical water heights at two measurement points: (a) H1 and (b) H2. Experimental data from [50].

particle method [53], smooth particle hydrodynamics (SPH) method [54], etc. have selected it as one of benchmark problems for their validation. On the other hand, the new dam-break experiment [50] provides longer time histories of not only the free surface but also the pressure measurements and has been also frequently cited for the validation of free surface methods in recent.

The dimensions of the tank are (3.22 m, 1.0 m, 2.0 m) in which the initial water column of (1.2 m, 1.0 m, 0.6 m) is placed behind the flap as shown in Figure 10. For comparison, we used the water heights measured by standard capacitive wave gauges at two probe points: H1 and H2 located 2.725 and 2.228 m from the left wall of the tank, respectively. Another available experimental result is the pressure history measured by using a circular pressure transducer of 0.9 m diameter

Copyright © 2009 John Wiley & Sons, Ltd.

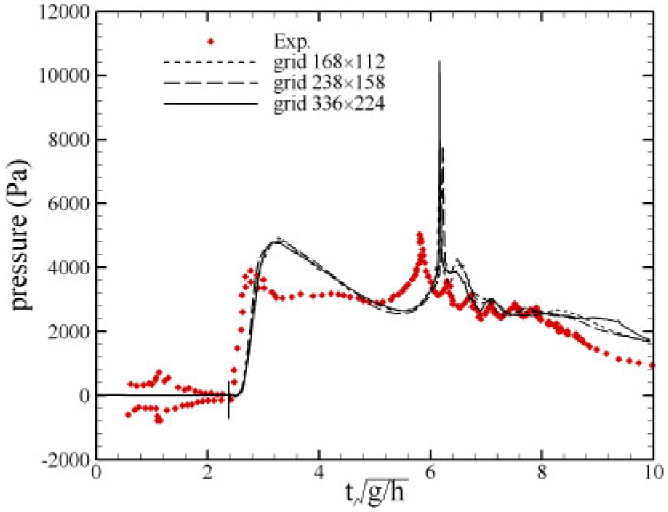

Figure 12. Pressure time history at a measurement point, P2 on the right wall. Experimental data from [50].

at a point P2, which is located 0.16 m from the bottom on the right wall of the tank. We assume the flow is ideally two-dimensional as in [55–57]. We numerically measured the water heights from the results in the same way as reported in [50, 56]. The final water heights were obtained by deducting the heights of the entrapped air cavities from the initial values. For the pressure comparison, we chose the value calculated at the bottom position of the pressure transducer as discussed in [57, 58].

In this numerical simulation, one challenging problem is to provide a reasonable accuracy even after the dimensionless time, $t\sqrt{g/h}\approx 6.0$, when the water reflected at the right wall overturns and meets the underlying free surface. We found that five different numerical methods had been applied to this test: a boundary element method [59, 60], a level-set method [55], one- and two-phase SPH methods [56], one- and two-phase VOF methods (SLIC) [58], and a one-phase VOF method (CICSAM) [57]. Especially, the three-dimensional results for this test can be found in [58]. All the methods provide almost identical solutions that are in a reasonable agreement with the experimental data as well, while $t\sqrt{g/h}<6.0$, but they begin to present divergent results when compared not only with each other but also with the experiment after $t\sqrt{g/h}\approx 6.0$. Although the results of non-viscous flow-based methods are still comparable with those of the viscous methods while $t\sqrt{g/h}<6.0$, it should be noted that the differences between numerical and experimental results are due to the limited information about the details of the experimental conditions (initial conditions and bottom roughness, etc.), as discussed in [56]. We include turbulence effects in our numerical simulations using a Reynolds-averaged turbulence model in which we do not consider an additional model for free surface fluctuation. We use the standard k-ε model with a wall function treatment [35] and locally refined grids for thin boundary layers.

For grid convergence study, we use three grid resolutions: a coarse grid (168×112), a medium grid (238×158), and a fine grid (336×224), where we put 30, 43, and 60 grid points within the thickness of 10 cm from the wall for each grid resolution, respectively. Here, we only consider the bottom and right walls of the tank for this non-uniform grid clustering. In each grid resolution,

Copyright © 2009 John Wiley & Sons, Ltd.

DOI: 10.1002/fld

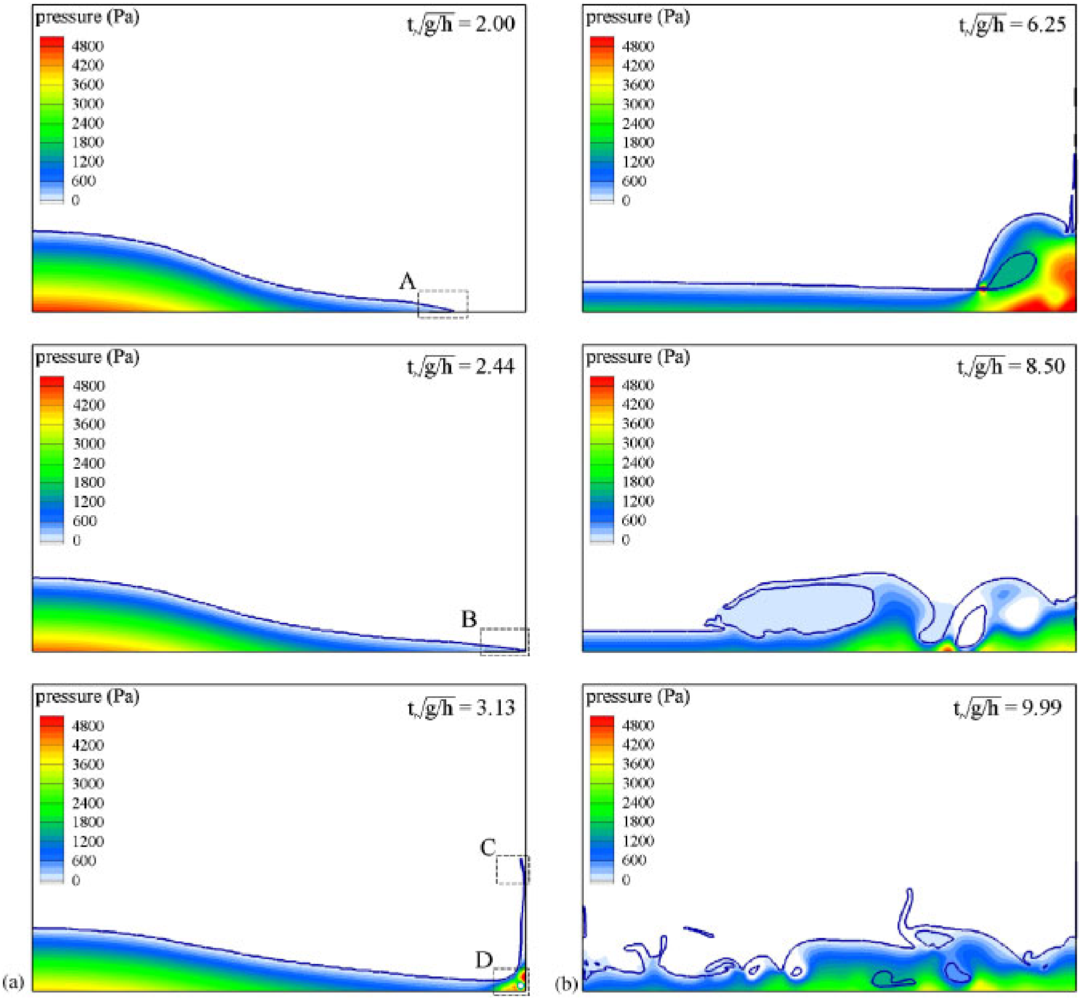

Figure 13. Time sequence of a dam-break: (a) $t\sqrt{g/h}=2.00$, 2.44, and 3.13 and (b) $t\sqrt{g/h}=6.25$, 8.50, and 9.99. Grid resolution is 336×224.

the corresponding distance of the first grid point to the wall is $1.60\mathrm{E}-4$, $1.13\mathrm{E}-4$, and $8.0\mathrm{E}-5$ m. Finally, these refinements let the variation of the maximum dimensionless distance $y^+(=u^\tau y/v)$ fall under about 120, 80, and 60 during the simulations, respectively, where $u^\tau(=\sqrt{\tau_w/\rho})$ is the friction velocity, v is the kinematic viscosity, and τ_w is the wall shear stress. We use a Courant number of 0.25 for this validation test and neglect the surface tension effects.

In Figure 11, we compare the water heights (h_w/h) at H1 and H2 probe points between succeeding grid resolutions, respectively. The present results are in satisfactory agreement with the measurements reported in [58, 50], except for the under-predictions of the sudden rise of the water at the initial stage, the phase lags, and slight over-predictions after $t\sqrt{g/h}\approx 6.0$. In Figure 12, we show the pressures measured and computed on the right vertical wall. Although over-predicted, our

Copyright © 2009 John Wiley & Sons, Ltd.

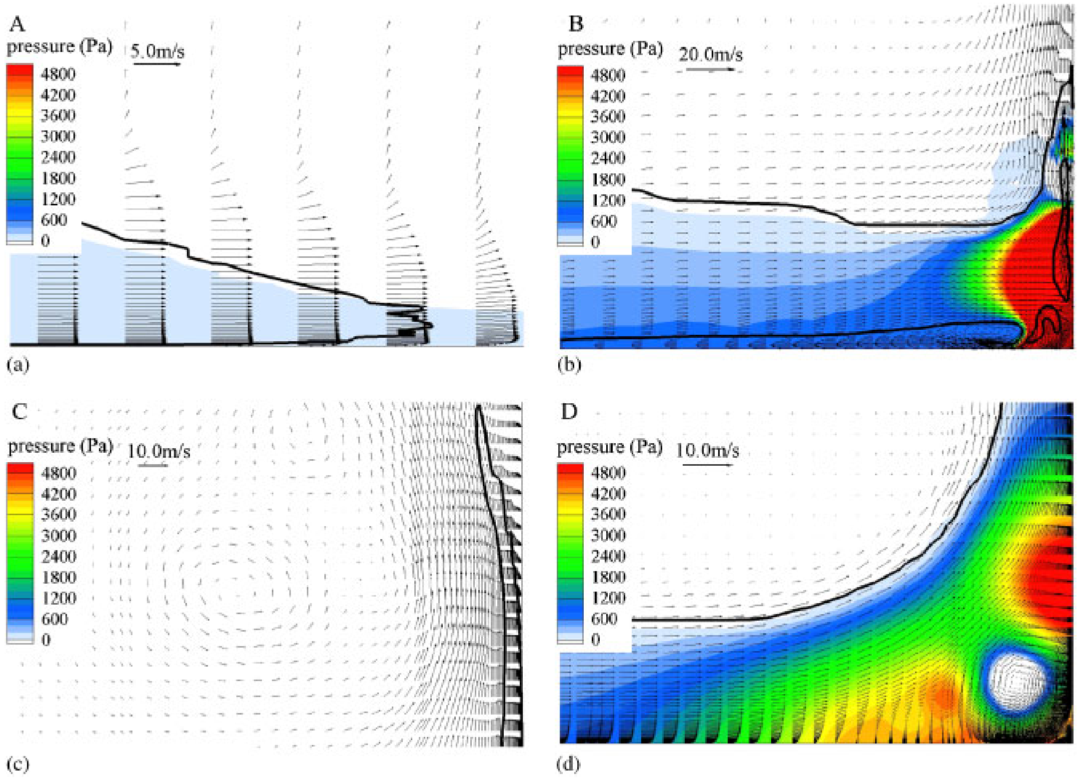

Figure 14. Magnified view of A, B, C, and D flow regions shown in (a) column of Figure 13: (a) A-region; (b) B-region; (c) C-region; and (d) D-region. Grid resolution is 336×224.

numerical results reproduce the first overshoot shown in the measurements as well as the second peak. For the pressure behavior after $t\sqrt{g/h}\approx 6.0$, the present simulation provides a slightly improved agreement with the measurements than other numerical results reported in the literature. In Figure 13, we display a sequence of snapshots of the water behaviors as the collapsed water impacts the right vertical wall and breaks up leftward. In Figure 14, we show the magnified views (A, B, C) of water front motions shown in Figure 13(a), (b), and (c) and the magnified snapshot (D) of the velocity and pressure distributions at the right bottom corner of the tank in Figure 13(c) after an instant when the first pressure peak occurs. In Figure 14(a), we show the very thin boundary layers developed on the bottom surface of the tank as well as the irregular-shaped water front. In this figure, we can also observe an interesting flow feature that the water front is detached from the wall surface because of the interactions of the inertia of the water and the wall friction forces. In Figure 14(b), we display an instant when the water jet impacts against the vertical wall and then separates into upward and downward, making a sudden rise of the pressure and including air entrainment. In Figure 14(c), we show the uprising water front along the vertical wall of the tank. Since the water front is under the influences not only of the gravity and its own inertia, but also of the wall friction forces, it is detached from the wall in a bent shape. In Figure 14(d), we show the formation of considerable vortices and the corresponding rapid pressure

Copyright © 2009 John Wiley & Sons, Ltd.

DOI: 10.1002/fld

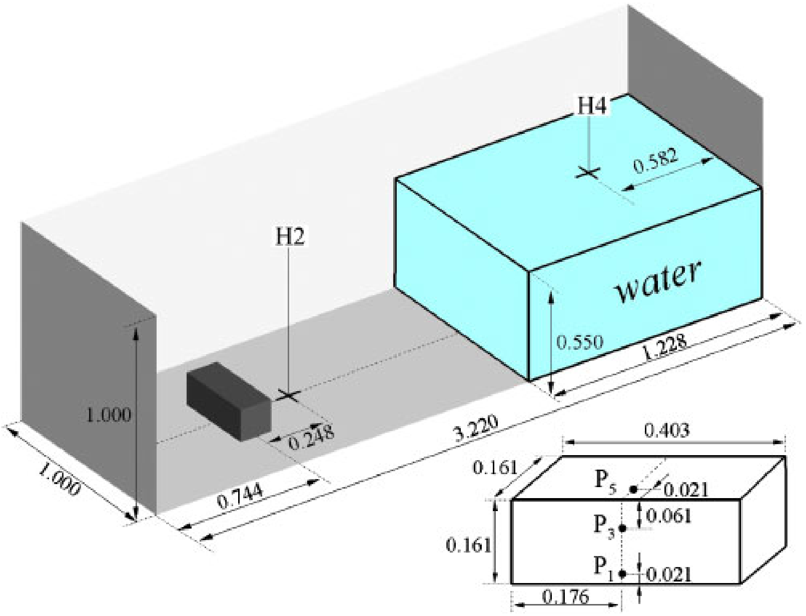

Figure 15. A three-dimensional dam-break over a rectangular box: problem definition and measurement points for water heights and pressures.

changes in the vicinity of the corner region when the water starts rising up after the impact of the water.

4.4. Three-dimensional dam-break over an obstacle

In this section, we test our implementation of VOF advection for a three-dimensional dam-break over a rectangular box performed by [5]. For this test case, the numerical results of a VOF method called as ComFLOW are also provided in the same Reference [5]. The dimensions of the tank are (3.22, 1.0, 1.0 m) in which the initial water column of (1.228, 1.0, 0.55 m) is placed behind a door that is opened by releasing a weight. The rectangular box is placed at a longitudinal distance of 0.744 m from the left wall of the tank. For comparison, we use the water heights at two probe points (H2, H4) in the tank and the pressures at three measurement points (P1, P3, P5) on the box surface as shown in Figure 15. We consider a half of the tank as the computational domain for this problem in which wall boundary conditions are given at all the surfaces of the tank and the box, except that a symmetry boundary condition is given at the center plane. For grid convergence test we use three grid resolutions: a coarse grid (115 920 CVs), a medium grid (375 221 CVs), and a fine grid (800 064 CVs), in which the distance of the first cell center point to the wall is the same value of 2.0E−4 m for each grid resolution. The same Courant number of 0.25 is used as in the previous two-dimensional dam-break simulations and the surface tension effects are neglected.

In Figure 16, we show a sequence of snapshots of the water behaviors. The collapsed water is suddenly rising up into the air after hitting the right face of the box in the three snapshots for times $t\sqrt{g/h}=2.01$, 2.87, and 4.00. Afterwards, the water returned from the left wall hits again the

Copyright © 2009 John Wiley & Sons, Ltd.

DOI: 10.1002/fld

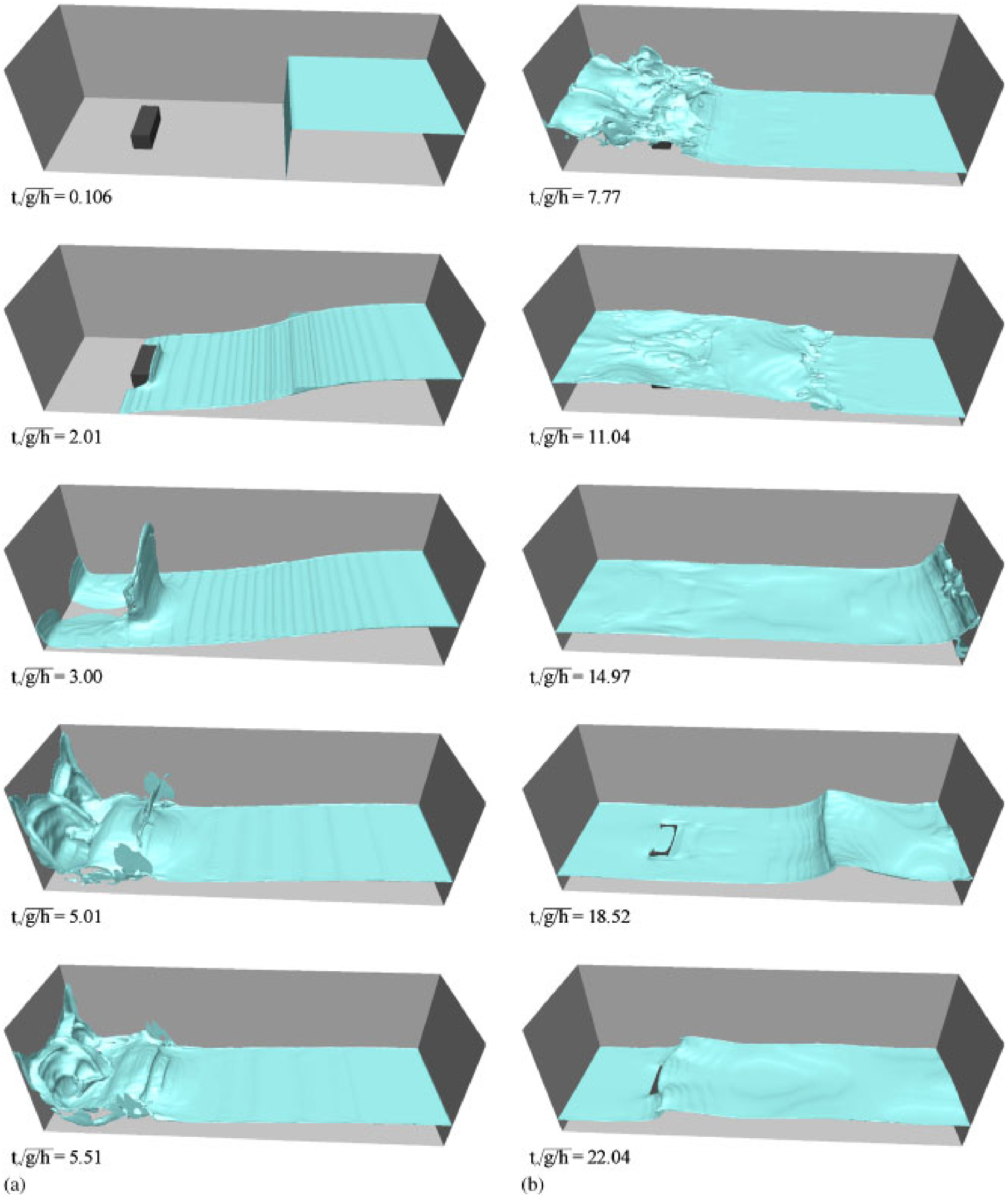

Figure 16. Time sequence of a three-dimensional dam-break: (a) $t\sqrt{g/h}=0.106$, 2.01, 3.00, 5.01, and 5.51 and (b) $t\sqrt{g/h}=7.77$, 11.04, 14.97, 18.52, and 22.04. Grid resolution is 800064 CVs.

Copyright © 2009 John Wiley & Sons, Ltd.

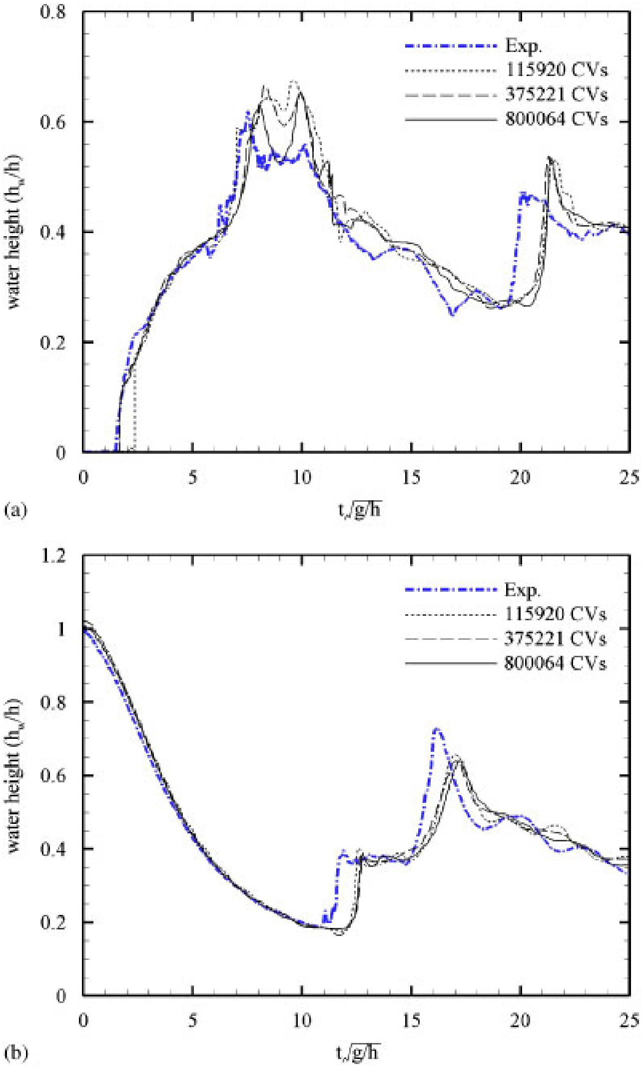

Figure 17. Vertical water heights at two measurement points: (a) H2 and (b) H4. Experimental data from [5].

back and top faces of the box and as a result, the water is bouncing up over the box into rightward direction. In the rest of the snapshots we display other sequent water behaviors: traveling, rising up along the right vertical wall of the tank, and the third hitting the box. In Figure 17, the water heights at H2 and H4 probe locations are compared. The present numerical results for three grid resolutions are in good agreement with the measurements and ComFLOW simulation results found in [5] except the phase lags after $t\sqrt{g/h}\approx 6.5$. Especially, after $t\sqrt{g/h}\approx 6.5$ the water violently breaks and on the water surface the free surface fluctuations are very severe, while under the water surface there are many air cavities. For the phase lag differences, which are also found in

Copyright © 2009 John Wiley & Sons, Ltd.

DOI: 10.1002/fld

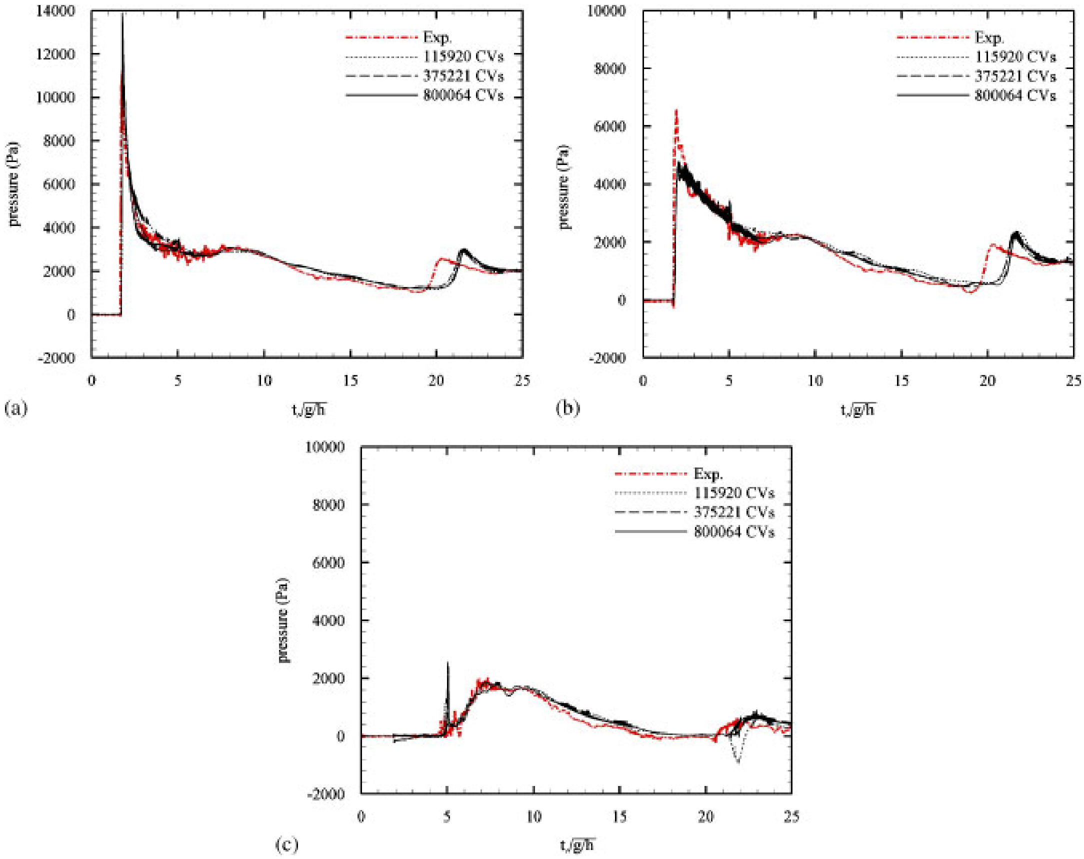

Figure 18. Pressure time histories at three measurement points on the box: (a) P1; (b) P3; and (c) P5. Experimental data from [5].

the previous two-dimensional dam-break case, it may be noted that the longitudinal flow speed is decelerated due to the increased numerical damping effects while the water violently breaks. The pressure histories at P1 and P3 points on the right face of the box and at P5 on the top of the box are compared in Figure 18. As for the water heights (h_w/h), the present solutions provide a very comparable agreement with the experimental data as well, except for the phase lag differences. The three moments of water hits on the box are clearly shown in all the numerical results in which the grid convergence also shows a good behavior. The agreements in time history and magnitude until $t\sqrt{g/h}\approx 10.0$ are very satisfactory although when compared with the measurements, the impact pressures are slightly over- and under-predicted at P1 and P3 probe points, respectively.

5. CONCLUSIONS

We developed a hybrid VOF level-set method for incompressible free surface flows. When considering surface tension, the level-set function is temporarily constructed from the VOF function in

Copyright © 2009 John Wiley & Sons, Ltd.

a straightforward way for improved accuracy in the interface normal and curvature calculations at every timestep. For this, specifically, a level-set distancing equation is solved using a fifth-order accurate discretization scheme in space that reduces the mass loss of the level-set function. The advection of the level-set function and a complicated geometric process to reconstruct the interface or to re-initialize the level-set function are not performed in this algorithm. For practical purposes, the present free surface method is developed so that it can be efficiently and easily extensible to three-dimensional structured grids with a minor implementation complexity. The proposed VOF method that is based on an algebraic algorithm for tracking the interface shows a nearly same order of accuracy with its comparable scheme sharing a similar volume advection algorithm. Furthermore, it is more comparable in accuracy to geometric interface reconstruction-based algorithms of higher accuracy than other interface capturing VOF methods. The numerical examples of a three-dimensional air bubble's rising in viscous liquids with a large density ratio show that the present hybrid algorithm provides a reliable accuracy in surface tension calculations, which is verified by comparing its results with those of two different front tracking methods. These tests also show that the mass conserved smooth level-set functions can be effectively obtained with the aid of the high-order differencing scheme for the level-set distancing equation and a smoothing process. Finally, the method is applied to a two-dimensional dam-break and a three-dimensional dam-break over an obstacle mounted on the bottom of a tank. In the two-dimensional dam-break, the numerical result computed using a Reynolds-averaged turbulence model and locally refined grids for boundary layers shows a slightly improved agreement with available experimental data than those from laminar flow assumption. Furthermore, the present simulation provides the local flow behavior of the deforming water front under the influence of viscous boundary layers, which have not been yet presented by other studies. It should be noted that further analysis is needed for complete understanding of the turbulence effects found in this test both experimentally and numerically. In the three-dimensional dam-break, the comparison of the free surface elevations and violent impacts of water on the fixed obstacle shows a good agreement between the numerical and experimental results, despite some phase differences that may be caused by numerical damping effects amplified during the water violently breaks.

ACKNOWLEDGEMENTS

This research was sponsored by the Ministry of Commerce, Industry, and Energy (MOCIE), Korea under the projects (PNS116D) and also partially supported by the basic research project at MOERI/KORDI (PES128A). We thank Dr Kleefsman of University of Groningen for providing the experimental data for the three-dimensional dam-break measured by the Maritime Research Institute Netherlands (MARIN).

REFERENCES

1. Hirt CR, Nichols BD. Volume of fluid (VOF) method for the dynamics of free boundaries. *Journal of Computational Physics* 1981; **39**:201–225.
2. Dommermuth DG, Sussman M, Beck RF, O'Shea TT, Wyatt DC, Olson K, MacNeice P. The numerical simulation of ship waves using Cartesian grid methods with adaptive mesh refinement. *Proceedings of the 25th Symposium on Naval Hydrodynamics*, St. John's, Newfoundland and Labrador, Canada, August 2004.
3. Fekken G, Veldman AEP, Buchner B. Simulation of green water loadings using the Navier–Stokes equations. *Proceedings of the Seventh International Conference on Numerical Ship Hydrodynamics*, Nantes, France, 1999.

Copyright © 2009 John Wiley & Sons, Ltd.

DOI: 10.1002/fld

4. Gerrits J. Dynamics of liquid-filled spacecraft. *Ph.D. Thesis*, University of Groningen, The Netherlands, 2001. Available from: www.ub.rug.nl/eldoc/dis/science/j.gerrits.
5. Kleefsman KMT, Fekken G, Veldman AEP, Iwanowski B, Buchner B. A volume-of-fluid based simulation method for wave impact problems. *Journal of Computational Physics* 2005; **206**:363–393.
6. Loots GE. Fluid–structure interaction in hemodynamics. *Ph.D. Thesis*, University of Groningen, The Netherlands, 2003. Available from: www.ub.rug.nl/eldoc/dis/science/g.e.loots.
7. Loots GE, Hillen B, Veldman AEP. The role of hemodynamics in the development of the outflow tract of the heart. *Journal of Engineering Mathematics* 2003; **45**:91–104.
8. Muzaferija S, Perić M, Sames P, Schellin T. A two-fluid Navier–Stokes solver to simulate water entry. *Proceedings of the 22nd Symposium on Naval Hydrodynamics*, Washington, DC, U.S.A., 1998.
9. Repetto RA. Computation of turbulent free-surface flows around ships and floating bodies. *Ph.D. Thesis*, Technical University of Hamburg, Harburg, 2001.
10. Wan DC, Wu GX. The numerical simulation of the green water effect. In *Proceedings of the 14th International Workshop on Water Waves and Floating Bodies*, Beck RF, Schultz WW (eds). National Academic Press: Washington, DC, 1999; 163–176.
11. Craft TJ, Kidger JW, Launder BE. Three dimensional modelling of turbulent free-surface jets. In *Engineering Turbulence Modelling and Measurements*, Rodi W, Laurence D (eds), vol. 4. Elsevier: Amsterdam, 1999; 73–82.
12. Dommermuth DG, Gharib M, Huang H, Innis GE, Maheo P, Novikov EA, Talcott JC, Wyatt DC. Turbulent free-surface flows: a comparison between numerical simulations and experimental measurements. *Proceedings of the 21st Symposium on Naval Hydrodynamics*, Trondheim, 1996; 249–265.
13. Sussman M, Almgren A, Bell J, Colella P, Howell L, Welcome M. An adaptive level set approach for incompressible two-phase flows. *Journal of Computational Physics* 1999; **148**:81–124.
14. Sussman M, Dommermuth D. The numerical simulation of ship waves using Cartesian grid methods. *Proceedings of the 23rd Symposium on Naval Hydrodynamics*, Val-De-Reuel, France, September 2000.
15. Scardovelli R, Zaleski S. Direct numerical simulation of free-surface and interfacial flow calculations. *Annual Review of Fluid Mechanics* 1999; **31**:567–603.
16. Noh W, Woodward P. SLIC—simple line interface calculation. In *Proceedings of the Fifth International Conference on Fluid Dynamics*, Vooren AV, Zandbergen P (eds). Lecture Notes in Physics, vol. 59. Springer: Berlin, 1976; 330.
17. Youngs DL. An interface tracking method for a 3D Eulerian hydrodynamics code. *Technical Report AWRE/44/92/35*, Atomic Weapons Research Establishment, 1987.
18. Harvie DJE, Fletcher DF. A new volume of fluid advection algorithm: the stream scheme. *Journal of Computational Physics* 2000; **162**:1–32.
19. Harvie DJE, Fletcher DF. A new volume of fluid advection algorithm: the defined donating region scheme. *International Journal for Numerical Methods in Fluids* 2001; **35**(2):151–172.
20. Lópeza J, Hernándezb J, Gómezb P, Faura F. An improved PLIC–VOF method for tracking thin fluid structures in incompressible two-phase flows. *Journal of Computational Physics* 2005; **208**:51–74.
21. Renardy Y, Renardy M. PROST: parabolic reconstruction of surface tension for the volume-of-fluid method. *Journal of Computational Physics* 2002; **183**:400–421.
22. Rudman M. A volume tracking method for interfacial flows with large density variations. *International Journal for Numerical Methods in Fluids* 1998; **28**:357–378.
23. Fluent. *Fluent 6.3 Users Guide*. Fluent Inc., 2006.
24. Kothe DB, Mjolsness RC. RIPPLE: a new model for incompressible flows with free surfaces. *AIAA Journal* 1992; **30**(11):2694–2700.
25. Lafaurie B, Nardone C, Scardovelli R, Zaleski S, Zanetti G. Modelling merging and fragmentation in multiphase flows with SURFER. *Journal of Computational Physics* 1994; **113**:134–147.
26. Leonard BP. The ULTIMATE conservative difference scheme applied to unsteady one-dimensional advection. *Computer Methods in Applied Mechanics and Engineering* 1991; **88**:17–74.
27. Maronnier V, Picasso M, Rappaz J. Numerical simulation of free surface flows. *Journal of Computational Physics* 1999; **155**:439–455.
28. Ubbink O, Issay RI. A method for capturing sharp fluid interfaces on arbitrary meshes. *Journal of Computational Physics* 1999; **153**:26–50.
29. Zalesak ST. Fully multi-dimensional flux corrected transport algorithms for fluids. *Journal of Computational Physics* 1979; **31**:335–362.
30. Bourlioux A. A coupled level-set volume-of-fluid algorithm for tracking material interfaces. *Proceedings of the Sixth International Symposium on Computational Fluid Dynamics*, Lake Tahoe, CA, 1995.

31. Son G. Efficient implementation of a coupled level-set and volume-of-fluid method for three-dimensional incompressible two-phase flows. *Numerical Heat Transfer B* 2003; **43**:549–565.
32. Sussman M, Puckett EG. A coupled level set and volume of fluid method for computing 3D and axisymmetric incompressible two-phase flows. *Journal of Computational Physics* 2000; **162**:301–337.
33. Sussman M, Smith KM, Hussaini MY, Ohta M, Zhi-Wei R. A sharp interface method for incompressible two-phase flows. *Journal of Computational Physics* 2007; **221**:469–505.
34. van der Pijl SP, Segal A, Vuik C, Wesseling P. A mass-conserving level-set method for modeling of multi-phase flows. *International Journal for Numerical Methods in Fluids* 2005; **47**:339–361.
35. Launder BE, Spalding DB. The numerical computation of turbulent flows. *Computer Methods in Applied Mechanics and Engineering* 1974; **3**:269–289.
36. Brackbill JU, Kothe DB, Zemach C. A continuum method for modeling surface tension. *Journal of Computational Physics* 1992; **100**:335–354.
37. Gaskell H, Lau AKC. Curvature compensated convective transport: SMART, a new boundedness preserving transport algorithm. *International Journal for Numerical Methods in Fluids* 1988; **8**:617–641.
38. Darwish MS, Moukalled FH. Normalized variable and space formulation methodology for high-resolution schemes. *Numerical Heat Transfer B* 1994; **26**:79–96.
39. Sussman M, Fatemi E, Smereka P, Osher S. An improved level set method for incompressible two-phase flows. *Computers and Fluids* 1998; **27**(5–6):663–680.
40. Ferziger JH, Perić M. *Computational Methods for Fluid Dynamics*. Springer: Heidelberg, 1996.
41. Khosla PK, Rubin SG. A diagonally dominant second-order accurate implicit scheme. *Computers and Fluids* 1974; **2**:207–209.
42. Van Leer BJ. Towards the ultimate conservative difference scheme. V. A second order sequel to Godunov's method. *Journal of Computational Physics* 1979; **32**:101–136.
43. Muzaferija S. Adaptive finite volume method for flow predictions using unstructured meshes and multigrid approach. *Ph.D. Thesis*, University of London, 1994.
44. Stone HL. Iterative solution of implicit approximations of multi-dimensional partial differential equations. *SIAM Journal on Numerical Analysis* 1968; **5**:530–558.
45. Patankar SV, Spalding DB. A calculation procedure for heat, mass and momentum transfer in three-dimensional parabolic flows. *International Journal of Heat and Mass Transfer* 1972; **15**:1787–1806.
46. Jiang G, Peng D. Weighted ENO schemes for Hamilton–Jacobi equations. *SIAM Journal on Scientific Computing* 2000; **21**:2126–2143.
47. Croce R, Griebel M, Schweitzer MA. A parallel level-set approach for two-phase flow problems with surface tension in three space dimensions, *Technical Report 157*, Sonderforschungsbereich 611, Universität Bonn, 2004.
48. Hao Y, Prosperetti A. A numerical method for three-dimensional gas–liquid flow computations. *Journal of Computational Physics* 2004; **196**:126–144.
49. Unverdi SO, Tryggvason G. A front-tracking method for viscous, incompressible, multi-fluid flows. *Journal of Computational Physics* 1992; **100**:25–37.
50. Zhou ZQ, De Kat JO, Buchner B. A nonlinear 3-D approach to simulate green water dynamics on deck. *Proceedings of the Seventh International Conference on Numerical Ship Hydrodynamics*, Nantes, France, 1999; 5.1–1, 15.
51. Martin JC, Moyce WJ. An experimental study of the collapsed liquid columns on a rigid horizontal plate. *Philosophical Transactions of the Royal Society of London Series A—Mathematical Physical and Engineering Sciences* 1952; **244**:312–324.
52. Ferreira VG, Kurokawa FA, Oishi CM, Kaibara MK, Castelo A, Cuminato JA. Evaluation of a bounded high order upwind scheme for 3D incompressible free surface flow computations. *Mathematics and Computers in Simulation* 2007. DOI: 10.1016/j.matcom.2007.04.018.
53. Koshizuka M, Oka Y. Moving particle semi-implicit method for fragmentation of incompressible fluid. *Nuclear Science and Engineering* 1984; **123**:421–434.
54. Violeau D, Issa R. Numerical modelling of complex turbulent free-surface flows with the SPH method: an overview. *International Journal for Numerical Methods in Fluids* 2007; **53**:277–304.
55. Colicchio G, Colagrossi A, Greco M, Landrini M. Free-surface flow after a dam break: a comparative study. *Ship Technology Research* 2002; **49**(3):95–204.
56. Colagrossi A, Landrini M. Numerical simulation of interfacial flows by smoothed particle hydrodynamics. *Journal of Computational Physics* 2003; **191**:448–475.
57. Nielsen KB. Numerical prediction of green water loads on ships. *Ph.D. Thesis*, Technical University of Denmark, 2003.

Copyright © 2009 John Wiley & Sons, Ltd.

DOI: 10.1002/fld

58. ten Caat M. Numerical simulation of incompressible two-phase flow. *Master's Thesis*, University of Groningen, 2002.
59. Greco M. A two-dimensional study of green-water loading. *Ph.D. Thesis*, Norwegian University of Science and Technology, 2001.
60. Greco M, Landrini M, Faltinsen OM. Impact flows and loads on ship-deck structures. *Journal of Fluids and Structures* 2004; **19**(3):251–275.

Copyright © 2009 John Wiley & Sons, Ltd.